

Integrated Propulsion System Analysis Framework for Designing Advanced Air Mobility Aircraft

Mohammad Irfan Alam, Zin Win Thu, Nghia Nguyen, Maxim Tyan, and Jae-Woo Lee

Abstract—Electric aircraft emerge as a promising solution to mitigate the environmental impact of the aviation sector. The integration of electric propulsion components in such aircraft differs significantly from that of conventional aircraft. In the latter case, initial sizing frameworks typically employ mathematical models that operate solely with high-level propulsion parameters, such as power, thrust, and efficiency. However, in the case of advanced air mobility (AAM) aircraft, the propulsion system integration at the sizing stage is critical to exploring more comprehensive configurations and avoiding infeasible solutions. We introduce a framework for designing AAM aircraft, emphasizing the crucial integration of propulsion components from the initial phase. It combines top-level, low-fidelity methods, higher-fidelity components, and system-level propulsion analysis. This modular approach facilitates realistic aircraft configuration exploration by efficiently balancing high and low-fidelity studies. This integrated approach significantly reduces the risk of infeasible or impractical solutions and allows for adaptable coupling with various models of differing fidelity. We demonstrate the framework's effectiveness by designing and analyzing a box-wing vertical takeoff and landing electric aircraft. Key results suggest setting the propeller pitch optimally at each mission segment increases the cruising range of aircraft by at least 10%. Similarly, varying the battery cell type with a fixed pack mass results in up to 10 km gain in cruising range for the optimal cruise speed. Propeller pitch, battery cell type, and other parameters are often omitted in the initial sizing stage. Our results emphasize the high sensitivity of aircraft performance to these parameters. The proposed framework illustrates its potential to advance electric aircraft design, contributing to a more sustainable future in aviation.

Index Terms—Electric vertical take-off and landing (eVTOL), urban air mobility (UAM), electric propulsion, sizing, modeling and analysis.

I. INTRODUCTION

Recent observations have highlighted a concerning rise in atmospheric CO₂ levels, a key factor driving global climate change [1]. In 2022, the Mauna Loa Observatory reported a record-high 418.56 parts per million (ppm) of CO₂, emphasizing the severity of this issue [2]. To mitigate these escalating concerns, global efforts are aligning with the Paris Agreement's goals, which include a 45% reduction in emissions by 2030 and reaching net-zero emissions by 2050 [3]. The aviation sector, responsible for nearly 1000 million tons of CO₂ emissions annually, is a critical area for intervention [4]. In this context, the advancement of electric aircraft for urban and regional transportation, collectively termed Advanced Air Mobility (AAM) - encompassing Unmanned Air Vehicles (UAV), Urban Air Mobility (UAM), and Regional Air Mobility

Konkuk Aerospace Design-Airworthiness Institute (KADA), Konkuk University, Seoul-05029, South Korea.



Fig. 1: Notable electric aircrafts: (a) eVTOL generation 6 by Wisk (Source: <https://wisk.aero/aircraft/>), (b) X-57 Maxwell by NASA (Source: <https://www.nasa.gov/aeronautics/x-57-maxwell/>), (c) Alice by Eviation (Source: <https://www.eviation.com/aircraft/>), (d) VoloCity by Volocopter (Source: <https://www.volocopter.com/en/urban-air-mobility>)

(RAM), is essential for sustainable air travel [5]. The industry's proactive engagement in AAM is demonstrated by various promising projects, as depicted in Fig. 1. The growing interest from academic and research institutions in this field is further evidenced by a significant increase in research activities, doubling in output compared to the previous year [6].

These exciting highlights indicate the critical momentum building behind these innovations. Moving to electric aviation for mass transportation involves complex challenges in design and operation, such as energy density, reliability, operational limits, and cost-effectiveness [7]. Additionally, AAM aircraft designs are more influenced by their specific design and mission needs compared to traditional aircraft. The need for standardized design and analysis methods in this new field and the confidential nature of contemporary projects further complicate the work of researchers and designers. Distributed Electric Propulsion (DEP) in electric aircraft is a key advantage, allowing for a wider variety of vehicle designs tailored to specific needs. An integrated framework is necessary to analyze different aircraft designs and choose components, especially regarding the propulsion system during the initial sizing phase.

Initial sizing plays a pivotal role in the preliminary stages of aircraft design, with researchers continually refining methods for advanced air mobility (AAM) aircraft. Over the past five years, the field has seen significant advancements, with several studies adapting standard sizing methods for conventional aircraft to better suit electric aircraft designs.

For instance, Donateo et al. [8] introduced a sizing method

specifically focused on electric propulsion for the lift-cruise UAM configuration. In contrast, Chakraborty and Mishra [9] explored sizing considerations for electric and hybrid aircraft with tilt-wing designs. The diversity within a single configuration is evident with multiple variations arising from Distributed Electric Propulsion (DEP) and varying degrees of hybridization in propulsion systems. In this context, de Vries et al. [10] and Saias et al. [11], presented preliminary sizing approaches for hybrid architectures in distributed propulsion systems. Additionally, Lee et al. [12] proposed a generic sizing approach tailored to UAM, demonstrating its effectiveness using Suave [13], a comprehensive aircraft design and analysis code under active development for several years.

Further contributions to the field include the work of Rendón et al. [14] and Abu Salem et al. [15], who conducted detailed analyses of the development challenges and issues associated with Hybrid Electric Aircraft (HEA). Their work highlights the importance of understanding the current status and challenges in propulsion system development with a focus on propulsion and energy management. Supporting this perspective, NASA's research [16] reported that an optimized propulsion system could reduce energy consumption by up to 25%.

While studies by Li et al. [17] and Ma et al. [18] provided specific analyses of propulsion systems, their focus was on aircraft without Electric Vertical Takeoff and Landing (eVTOL) and DEP. Nonetheless, these studies offer valuable insights for our research. Additionally, some of the research efforts [19, 20, 21] have concentrated on component-level analyses, contributing significantly to our understanding of electric aircraft systems. Works by Wu et al. [22], Chauhan and Martins [23] investigate the interactions between wings and propellers, offering detailed aerodynamic modeling insights. These studies are instrumental in comprehensively analyzing designed configurations. Moreover, research in [24, 25, 26, 27] have provided in-depth system modeling and analysis approaches, primarily developed for UAVs yet applicable in broader contexts.

In the design of Advanced Air Mobility (AAM) aircraft, the initial sizing phase often overlooks the crucial aspect of propulsion feasibility. This common oversight can lead to impractical or suboptimal aircraft dimensions, requiring frequent adjustments to accommodate the varying impacts of different component choices. Traditional methods, typically used in a standalone manner, further complicate this issue. They lack the detailed mathematical modeling necessary for a robust and flexible design process, which limits the exploration of diverse configurations and accurate estimations.

To address this gap, there is a clear need for a comprehensive system-level approach. Such an approach should not only focus on vehicle sizing but also seamlessly integrate component-level analysis, particularly of the propulsion system. This integration requires a modular and adaptable framework, allowing for a more holistic and efficient design process that can accommodate a wide range of aircraft configurations and propulsion options.

We present an integrated framework that effectively combines component-level propulsion analysis with aircraft sizing

considerations, addressing the previously identified gap in Advanced Air Mobility (AAM) design. This approach ensures robustness and adaptability in the design process. Our framework starts with a detailed sizing method, progresses to comprehensive mathematical modeling for propulsion components, and then integrates these elements cohesively. We demonstrate its effectiveness through application to our in-house box-wing UAM aircraft currently under development. This framework facilitates exploration of diverse configurations and ensures feasibility through extensive analyses and optimizations before finalizing design choices.

Our novel framework is systematic, modular, and well-suited for complex aircraft propulsion challenges. Its adaptability and flexibility allow for component interchangeability and analysis modifications to suit specific design needs, enhancing its relevance in the evolving field of aircraft design. The subsequent sections detail our framework: Section II presents the overall description; Section III outlines the propulsion system analysis and its mathematical modeling; Section IV focuses on validating our methodology at the component level; and Section V applies our framework to a fully electric UAM aircraft case study, illustrating the results.

II. PROPOSED FRAMEWORK

Our proposed framework integrates the sizing method with propulsion analysis, consisting of four distinct modules: preliminary data, initial sizing, secondary loop, and the propulsion system, as depicted in Fig. 2. The process begins with prior information, where we collect the requirements based on market analysis or direct customer feedback. This stage involves refining design requirements and conducting a thorough mission analysis, mindful of relevant regulations and fixed parameters like physical constants and technological constraints.

The second module, viz., initial sizing, is pivotal in estimating the weight and size of the aircraft's components. This step sets baseline dimensions in alignment with the design and mission specifications, calculating the total mass, including the structure, systems, payload, and propulsion. A crucial decision point here is 'Mass Convergence': a checkpoint for mass estimation alignment with design objectives. The iterative process continues until this convergence is achieved.

Upon achieving satisfactory initial sizing, we advance to the detailed configuration phase. It includes precise component placement and integration, moving us into the performance analysis module. This iterative process further refines the vehicle's design, encompassing aerodynamic coefficient estimation and overall performance assessment. The propulsion analysis module is coupled to evaluate performance under various flight conditions, ensuring it meets the necessary criteria.

The output from this process encompasses detailed performance metrics such as thrust, torque, battery status, and propeller performance, including range and other essential parameters. Our framework ensures a comprehensive consideration of all aircraft design aspects, judiciously choosing them to fulfill the specified requirements and design objectives. As the figure details, we interconnect the modules through a feedback loop. It facilitates the refinement of aircraft sizing, enabling the

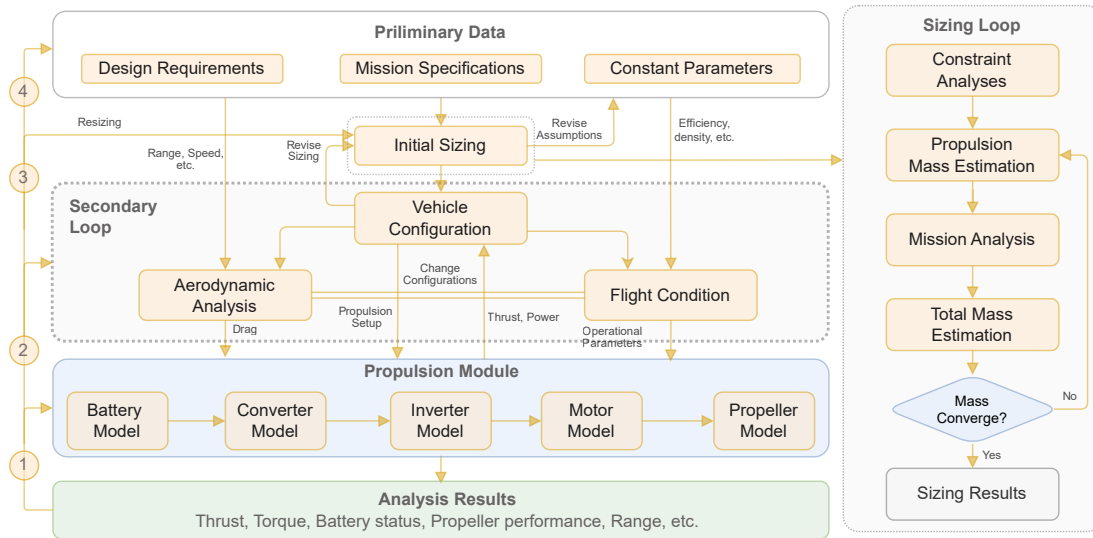


Fig. 2: Proposed integrated sizing and propulsion system analysis framework

selection and substitution of components with precision. The analysis results are connected back to the propulsion analysis module and operate at various levels, viz., ① for propulsion adjustments, ② for vehicle adjustment, ③ for resizing, and ④ for change in design requirements, mission specifications, or constant parameters. This hierarchical approach ensures that changes at any level are systematically evaluated for their impact on the overall design, allowing for a thorough and iterative refinement process. The interplay between these levels means that even minor adjustments at the component level can lead to significant modifications in the system, thus underlining the importance of each module within our integrated framework. This structure is instrumental in ensuring that the final aircraft design is feasible and aligned with the specific requirements and objectives set forth at the outset. Here, we discuss the mathematical modeling involved in the sizing and performance analysis. We discuss the propulsion analysis module in the next section.

The integration of aerodynamics and propulsion analysis within our framework takes into account how ambient air density changes with altitude, directly affecting lift, drag, and thrust generation. This crucial detail ensures that our design process dynamically interacts with flight conditions, highlighting the framework's ability to adapt and refine based on operational environments. This approach not only optimizes performance but also ensures the aircraft design is robust and responsive to varying atmospheric conditions.

A. Initial Sizing

Using the preliminary data, we initiate the sizing process with constraint analysis to define the feasible design region, focusing on critical parameters such as power-to-weight ratio, disc loading, and wing loading, all aligned with the aircraft's performance requirements. This analysis informs the calculation of the propulsion system mass, considering the established power-to-weight ratio and disc loading.

Following this, we conduct a mission analysis tailored to specific mission requirements, which then guides the sizing of the battery energy system based on the calculated energy needs and maximum power requirements. The final step involves computing the total takeoff mass. This is achieved by considering the mass fraction assumption alongside the payload, battery, and electronic components' mass.

We implement a mass convergence iteration using the fixed-point iteration method to ensure accuracy and feasibility. If convergence is achieved, it signifies that the aircraft is correctly sized. We then optimize the design to minimize the maximum takeoff mass, ensuring a feasible and efficient aircraft design.

Our sizing methodology, detailed in Table I, employs a blend of classical and modified equations to establish the fundamental relationships necessary for aircraft design. We utilize classical performance constraint equations for forward flight aircraft [30] to determine the correlation between wing and power loading. Additionally, we incorporate classical rotorcraft equations [31] and modified constraints [28] to size the wing area and propulsion system components accurately, based on the interplay of wing loading, disc loading, and the power-to-weight ratio. A total of six constraints guide our analysis, focusing on power-to-weight ratio, wing loading, and disc loading.

For the propulsion system, we estimate the mass based on the power-to-weight ratio and disc loading derived from the constraint analysis. This estimation includes the propeller, motor, inverter, and converter components. Mass calculations for the motor, inverter, and converter are grounded in a regression model of existing products, as shown in Table I. We do not size components like motor casings and cooling systems separately. Instead, our model, inherently accounts for these elements, ensuring a comprehensive representation of motor characteristics in our analysis. The propeller diameter is estimated using Raymer's method [32] and from disc loading

TABLE I: Sizing method and related equations

Analysis	Name	Equation
Constraint analysis	Stall Speed	$W/S = \frac{1}{2} V_{stall}^2 \rho C_{Lmax}$
	Cruise Speed	$P/W_{cruise} = (qC_{D0} \frac{1}{W/S} + k \frac{1}{q} W/S) \frac{V_{max}}{\eta_{prop}}$
	Rate of climb	$P/W_{ROC} = (\frac{ROC}{V_{ROC}} + \frac{q}{W/S} C_{D0} + \frac{k}{q} (W/S)) \frac{V_{ROC}}{\eta_{prop}}$
	Serve ceiling	$P/W_{serv} = (\frac{0.5}{V_{ROC}} + \frac{q_{serv}}{W/S} C_{D0} + \frac{k}{q_{serv}} (W/S)) \frac{V_{ROC}}{\eta_{prop}}$
	Hovering [28]	$P/W_{hover} = \sqrt{\frac{W/A}{2\rho} \frac{1}{FOM}}$
	Takeoff & landing [28]	$P/W_{VTOL} = \frac{f_p V_{VTOL}^2 + W/S}{W/S - f_w W/A}$ $[(2 - k_i) \frac{V_{VTOL}}{2} + k_i \sqrt{(\frac{V_{VTOL}}{2})^2 + \frac{W/A}{2\rho} \frac{f_p V_{VTOL}^2 + W/S}{W/S - f_w W/A}}]$ $+ \frac{\rho V_{tip}^3}{W/A} (\frac{\sigma C_d}{8})$
Propulsion mass sizing	Propeller mass	$M_{prop} = 27.59 D_{prop} - 38.457$
	Motor mass	$D_{prop} = \max\{D_{prop_{power}}, D_{prop_{VTOL}}\}$
	Inverter/Converter mass	$M_{motor} = 0.208 P_{motor} + 4.629$
	Propulsion estimation [29]	$M_{inv/conv} = 0.055 P_{inv/conv} + 1.721$
		$M_{propulsion} = f_{inst} N_{prop} (M_{prop} + M_{motor} + M_{inv} + M_{conv})$
Mission analysis	Power required	$P_{req_i} = P/W_i W \forall i \in N, N$ is the mission profile
	Energy required	$E_{req_i} = P_{req_i} t_i \forall i \in N, N$ is the mission profile
	Energy required total	$E_{req_{mission}} = \sum_i^N E_{req_i}$
Battery mass estimation	Battery mass	$M_{batt} = \max\{M_{P^*}, M_{E^*}\}$
		$M_{P^*} = \frac{P_{max_{batt}}}{P^*}$
		$M_{E^*} = \frac{E_{req_{mission}}}{DoD E^* \eta_{batt}}$
Total mass estimation	Maximum takeoff mass	$MTOM = \frac{M_{propulsion} + M_{battery} + M_{payload}}{1 - M_{Fairframe}}$

results. Considering the tilting mechanism of our system, we use the maximum diameter to avoid undersizing the propulsion mass.

Our mission analysis quantifies the power and energy requirements, guided by the mission profile's demands. Power needs are calculated using equations from our constraint analysis, multiplied by the maximum takeoff weight. This figure is then multiplied by mission segment durations to ascertain the energy required for each segment and the total flight mission.

In our selection process for the battery, we prioritize specific power and energy to ensure the choice aligns with both the maximum power output and mission energy demands, as emphasized by Brelje and Martins [33]. This approach prevents undersizing, which could compromise power availability and operational range, and oversizing, which may lead to unnecessary weight and increased costs, detrimentally impacting aircraft efficiency and performance. During the battery sizing, we account for both the cell mass and the additional weight from the casing and other components, integrating a battery packing efficiency factor for accuracy. Additionally, we incorporate a typical Depth of Discharge (DoD) of about 80% into our calculations to account for safety considerations in our designs.

B. Performance Analysis

We use a two-degree-of-freedom (2-DOF) model based on point-mass-based equations of motion to calculate aircraft performance, as illustrated in Fig. 3. Specifically, the equation of motion for tilting in vertical flight mode is derived under Newton's second law of motion. This derivation assumes steady rotation about the aircraft's center of gravity and considers

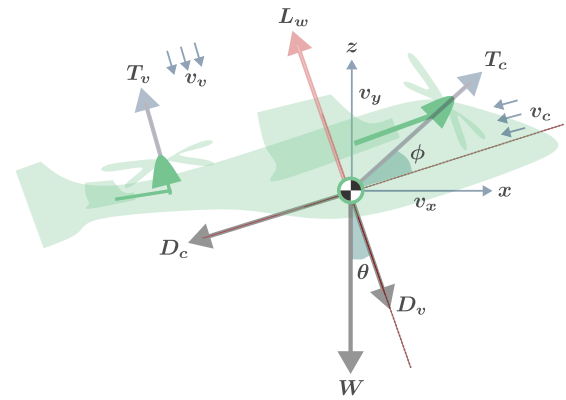


Fig. 3: Force balance of aircraft

a small angle of attack, where $(\alpha \approx 0)$. This simplification allows us to focus on the essential dynamics of tilting during vertical flight for aircraft performance calculations.

Concerning the figure, forces parallel and perpendicular to the flight path can be resolved as follows:

$$\frac{W}{g} \frac{dv_c}{dt} = T_c \cos \phi - D_c - W \sin \theta \quad (1)$$

$$\frac{W}{g} \frac{dv_v}{dt} = T_v + L_w - W \cos \theta + T_c \sin \phi \pm D_v \quad (2)$$

Here, T_c represents the thrust generated by the tilting propeller, and T_v denotes the thrust of the vertical propeller. L_w is the lift force, while D_c and D_v are the drag forces during forward and vertical flight, respectively. The variables ϕ and θ represent the tilting and flight path angles, respectively. These equations form the basis for understanding the dynamics of the aircraft as

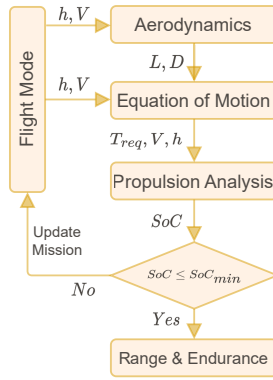


Fig. 4: Performance and mission analysis

it maneuvers through different flight modes, considering both the tilting and vertical propulsions in relation to the aircraft's orientation and trajectory.

We carry out performance and mission analysis by solving the equations above of motion tailored to different flight modes. The flow of this performance analysis is depicted in Fig. 4. We conduct aerodynamic analysis based on specific flight modes, considering factors such as altitude and airspeed. This analysis facilitates the calculation of the required thrust for propulsion and mission analysis.

We estimate the required thrust through aerodynamic analysis depending on the flight mode. Lift and drag are expressed as:

$$L_w = \frac{1}{2} \rho V^2 S C_L \quad (3)$$

$$D = \frac{1}{2} \rho V^2 S C_D \quad (4)$$

For forward flight, we estimate the drag coefficient using friction codes for friction drag and AVL for lift-induced drag:

$$C_{D_c} = C_{D_0}(V, h) + C_{D_i}(V, h) \quad (5)$$

In vertical flight, where $(\alpha = 90^\circ)$, the drag coefficient is approximated based on flat plate theory:

$$C_{D_v} \approx 2 \sin^3 \alpha \approx 2 \quad (6)$$

We then detail the thrust estimation and assumptions for each flight mode:

a) *Vertical Takeoff and Landing Mode*: Characterized by steady takeoff and no forward motion with $V_c = 0$, $\phi = 90^\circ$, $\theta = 0^\circ$ and $V_v = V$. Assuming no acceleration during takeoff and no forward flight motion, the equation simplifies to:

$$T_v + T_c = W \pm D_v \quad (7)$$

b) *Hovering Flight Mode*: Defined by no motion in either forward or vertical directions with $V_c = 0$, $\phi = 90^\circ$, $\theta = 0^\circ$ and $V_v = 0$. The equation of motion then becomes:

$$T_v + T_c = W \quad (8)$$

TABLE II: Transition: Initial and final conditions

Parameter	Start Condition	End Condition
V_c	0	$1.2V_{stall}$
T_v	$W/2$	0
T_c	$W/2$	$W/2$
L	0	W
ϕ	90°	0
θ	0	0

c) *Climb and Descent Mode*: In steady climb or descent, represented by $V_c = V_{ROC}$, $\phi = 0^\circ$, $\theta = \theta^\circ$ and $V_v = 0$. We solve two equations using fixed-point iteration to determine θ for any given airspeed:

$$T_c - D_c = W \sin \theta \quad (9)$$

$$L = W \cos \theta \quad (10)$$

d) *Transition Flight Mode*: The transition segment, albeit brief, involves complex analysis due to the shift from hovering to cruising. To address this, we set boundary conditions at both the start and end of the transition. The transition initiates in a hovering state and concludes in a cruising condition, where the cruise speed exceeds the stall speed. During this phase, the tilting angle and vertical thrust are gradually reduced, facilitating the aircraft's acceleration while maintaining its flight altitude. Table II lists the boundary conditions for the flight parameters.

The equations of motion for the transition flight are expressed as follows:

$$\frac{W}{g} a = T_c \cos \phi - D_c \quad (11)$$

$$0 = T_v + L - W + T_c \sin \phi \quad (12)$$

From these equations, the required thrust can be calculated as:

$$T_c = \frac{\frac{W}{g} a + D_c}{\cos \phi} \quad (13)$$

$$T_v = W - L - T_c \sin \phi \quad (14)$$

These formulations are critical in understanding and calculating the thrust dynamics during the intricate transition from vertical to forward flight. Next, we discuss the modeling of the propulsion system analysis module.

III. PROPULSION ANALYSIS

The electric propulsion system is pivotal in designing, developing, and operating electric aircraft. This section details our methodology for analyzing the electric propulsion system in electric aircraft. Fig. 5 displays a simplified depiction of the distributed electric propulsion (DEP) architecture, a key element in all-electric aircraft design. It emphasizes the modular nature of the DEP system, highlighting its adaptability and the ease with which components can be modified or exchanged based on specific design requirements. It also enables precise performance assessment and facilitates the customization of

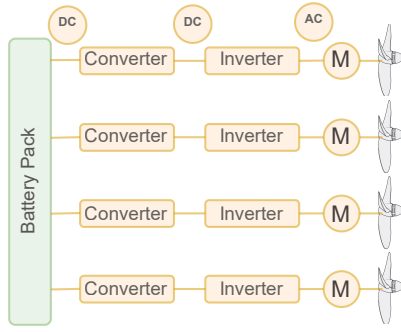


Fig. 5: Electric propulsion system

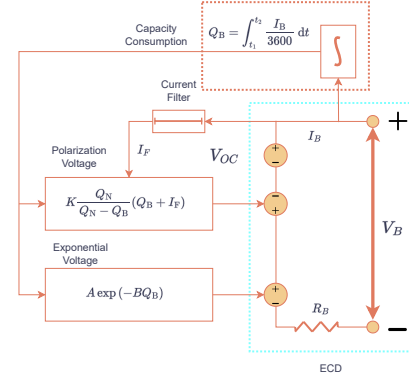


Fig. 6: Battery model equivalent circuit diagram

component selection, ensuring optimal alignment with particular design and mission requirements.

These components are depicted in a linear configuration, symbolizing the power flow from the battery pack through the converters, inverters, and ultimately to the motors. The converters are responsible for adjusting the DC power from the battery pack, while the inverters convert this power to AC, suitable for the motors. Each motor is linked to a propeller, representing the propulsion mechanism of the aircraft. Now, we discuss the model corresponding to each component.

1) *Battery Model*: Accurate State of Charge (SoC) estimation is crucial for estimating aircraft performance. Various battery models have been discussed in literature, each with its own merits. Electrochemical mechanism models are highly accurate but complex, making them more suitable for battery design and manufacturing. Data-driven models, especially those based on neural networks, require extensive training data, leading to higher computational costs. Reviews by Zhou et al. [34] and Wang et al. [35] provide in-depth insights into these battery modeling techniques.

Equivalent Circuit Model (ECM)-based models offer an optimal balance between complexity and accuracy, making them preferred choices for real-world applications [26, 36]. While Thevenin and other battery models provide higher accuracy, around $\pm 1\%$ [37, 38, 39], our framework utilizes a modified version of the ECM, depicted in Fig. 6. This model is selected for its speed, robustness, and reasonable accuracy [40]. It simplifies the parameterization process using inputs derived from discharge characteristics or manufacturer data and is adaptable to a variety of battery chemistries and configurations. The modular nature of our framework also allows for easy integration of alternative models, offering the flexibility needed to adapt to different scenarios.

Fig. 7 presents the typical discharge curve of a Li-Ion battery, capturing three distinct regions. Initially, there's a rapid voltage drop, termed the exponential region, followed by the nominal region, where voltage stabilizes, offering consistent power output. Finally, the voltage sharply decreases to the cut-off point, indicating the battery's minimum usable limit to prevent damage. The horizontal axis measures the battery's storage capacity in Ampere-hours (Ah), marking the top, nominal, and maximum capacity, respectively, with a steep voltage decline signifying depletion and the need for recharging.

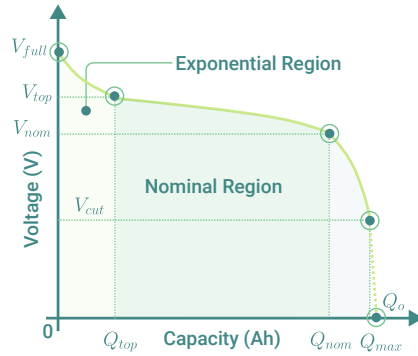


Fig. 7: Typical discharge curve of a battery

We use a model incorporating polarization voltage as a time-dependent state variable, accounting for variations in output voltage [40]. The discharge voltage is estimated using the following equation:

$$V_B = \underbrace{V_C - R_B I_B}_{\text{Equivalent circuit}} - \underbrace{K \frac{Q_N}{Q_N - \int_{L_1}^{t_2} \frac{I_B}{3650} dt}}_{\text{Polarization}} \left(\int_{t_1}^{t_2} \frac{I_B}{3600} dt + I_F \right) + \underbrace{A \exp \left(-B \int_{t_1}^{t_2} \frac{I_B}{3600} dt \right)}_{\text{Exponential}} \quad (15)$$

Here, A is the amplitude of the exponential zone (V), B is the inverse time constant, Q_N is the nominal battery capacity (Ah), R_B is the internal resistance (Ω), K is the polarization constant, V_C is the battery's constant voltage, and V_B is the terminal voltage. I_F and I_B denote the filtered and battery currents, respectively. The coefficients A and B are defined as follows:

$$A = V_F - V_C + R_B I_B, \quad B = \frac{3}{Q_E} \quad (16)$$

To determine the polarization constant K , we use the following equation, considering maximum charge (Q_{max}), nominal charge (Q_N), and other battery parameters:

$$K = -\frac{(Q_{\max} - Q_N)[V_N - V_C + R_B I_B - A \exp(-BQ_N)]}{Q_{\max}(Q_N + I_B)} \quad (17)$$

We estimate the SoC using the following expression:

$$\text{SoC} = \frac{Q_{\max} - \int_{t_1}^{t_2} \frac{I_B}{3600} dt}{Q_{\max}} \times 100 \quad (18)$$

Regarding the physical arrangement of batteries, they can be configured in either series-parallel or parallel-series connections to achieve the desired pack voltage and current. The total pack voltage (V_{pack}) and current (I_{pack}) can be calculated as follows, where N_S and N_P are the numbers of series and parallel connections, respectively:

$$V_{\text{pack}} = V_B N_S \quad (19)$$

$$I_{\text{pack}} = I_B N_P \quad (20)$$

2) *Converter Model*: A DC-DC converter is an integral component in power supply applications, serving to adapt the voltage level of a DC source to meet the requirements of various devices. Such converters are pivotal in managing energy flow in systems where source and load voltages differ. They are commonly utilized for voltage regulation in energy storage systems and portable electronic devices, among other applications [41]. This study focuses on buck converters due to their relevance in electric propulsion systems, particularly in eVTOLs. High-voltage batteries or fuel cells employed in eVTOLs necessitate buck converters to step down the voltage to suitable levels for motors, avionics, and other electric devices.

The efficiency of a buck converter is a critical aspect directly influenced by the power losses occurring within its components, namely the MOSFET, diode, and inductors. These losses are quantified using the ensuing equations:

$$D = \frac{V_{\text{in,conv}}}{V_{\text{out,conv}}} \quad (21)$$

where D represents the duty cycle of the converter, a unitless parameter that determines the output voltage ($V_{\text{out,conv}}$) and ($V_{\text{in,conv}}$) is the input voltage. The duty cycle is instrumental in calculating the power losses in both the MOSFET and the diode, which can be determined using Equations 22 and 23.

$$P_{M,\text{conv}} = I_{\text{out,conv}}^2 \cdot R_{\text{ds(on)}} \cdot D \quad (22)$$

$$P_{D,\text{conv}} = I_{\text{out,conv}} \cdot (1-D) \cdot V_{\text{fw}} + I_{\text{out,conv}}^2 \cdot (1-D) \cdot R_d \quad (23)$$

Inductor losses can be calculated from the output current ($I_{\text{out,conv}}$) and inductance of the converter (R_L):

$$P_{L,\text{conv}} = I_{\text{out,conv}}^2 \cdot R_L \quad (24)$$

The cumulative loss within the converter aggregates the losses from the MOSFET, diode, and inductor components:

$$P_{\text{losses,conv}} = P_{M,\text{conv}} + P_{D,\text{conv}} + P_{L,\text{conv}} \quad (25)$$

Finally, the input current ($I_{\text{in,conv}}$) to the converter is computed as the quotient of the input power and the input voltage:

$$I_{\text{in,conv}} = \frac{P_{\text{out,conv}} + P_{\text{loss,conv}}}{V_{\text{in,conv}}} \quad (26)$$

It is essential to account for all types of losses to ensure the accurate prediction of the converter's performance. These losses directly impact the efficiency and thermal management of the converter, which are crucial for the reliable operation of eVTOLs.

3) *Inverter Model*: A three-phase inverter is used to convert DC into AC for powering a Permanent Magnet Synchronous Motor (PMSM). In our analysis, we focus on the efficiency of this inverter, which employs Gallium Nitride (GaN) Metal-Oxide-Semiconductor Field-Effect Transistors (MOSFETs). GaN-MOSFETs are recognized for their high efficiency, largely due to their low on-state resistance and higher switching speed [42]. These properties enable the development of smaller and lighter inverters, essential in aerospace applications. Despite their relatively recent emergence, the rapid advancements in GaN technology [43, 44] make them a promising choice.

A critical factor in inverter efficiency is the conduction losses of GaN-MOSFETs, which constitute a significant portion of total power losses. We simplify the assessment by focusing on conduction losses and omitting switching losses, which are generally low for GaN devices. The conduction losses are quantified using the phase current ($I_{\phi,\text{inv}}$) and the MOSFET's on-state resistance ($R_{\text{ds(on)}}$). Additionally, the modulation index (m_a) and the phase angle (ϕ) are crucial to the calculation, representing the inverter's operating conditions and the power factor of the load, respectively.

$$P_{M,\text{inv}} = I_{\phi,\text{inv}}^2 \cdot R_{\text{ds(on)}} \cdot \left(\frac{1}{8} + \frac{m_a \cdot \cos(\phi)}{8} \right) \quad (27)$$

$$P_{D,\text{inv}} = I_{\phi,\text{inv}} \cdot V_{\text{fw}} \cdot \left(\frac{1}{2\pi} - \frac{m_a \cdot \cos(\phi)}{8} \right) + I_{\phi,\text{inv}}^2 \cdot \left(\frac{1}{8} - \frac{m_a \cdot \cos(\phi)}{3\pi} \right) \cdot R_d \quad (28)$$

The total conduction losses within the inverter are obtained by summing the losses from the MOSFETs and diodes:

$$P_{\text{loss,inv}} = 6 \cdot (P_{M,\text{inv}} + P_{D,\text{inv}}) \quad (29)$$

Subsequently, the input power and current to the inverter ($I_{\text{in,inv}}$) can be determined to provide insight into the overall efficiency of the power conversion process:

$$P_{\text{in,inv}} = P_{\text{loss,inv}} + P_{\text{out,inv}} \quad (30)$$

$$I_{\text{in,inv}} = \frac{P_{\text{in,inv}}}{V_{\text{DC}}} \quad (31)$$

This analytical approach enables the quick estimate of the inverter's efficiency. In the next section we describe the motor modeling.

4) *Motor Model*: Electric motors are an integral part of electric aircrafts. They are responsible for converting electrical energy into mechanical energy, providing propulsive force necessary for flight. UAM aircraft while going through various flight phases, require motors that can deliver high torque within a confined speed range. This is distinct from the automotive industry's focus on high-speed motors for electric vehicles (EVs) [45].

For our eVTOL aircraft propulsion, we've chosen Permanent Magnet Synchronous Motors (PMSMs) over Brushless DC Motors (BLDC) due to their superior compactness, high torque density [46] and rapid response to load changes [47], Tessential for eVTOL's varying flight demands. PMSMs offer greater efficiency, lower noise, and improved power density, despite their higher cost and complex control requirements [48, 49]. These features make PMSMs the optimal choice for achieving the performance goals of our eVTOL aircraft design, ensuring it meets the high standards required for efficient and effective propulsion.

Figure 8 represents a simplified equivalent circuit model of a PMSM. The stator resistance R_s and synchronous inductance L_s are parameters obtained from motor manufacturers. For analyzing the motor's performance, phasor analysis within the d-q reference frame is employed, as suggested by [50]. The rotor's magnetic field establishes the d-axis as the reference axis.

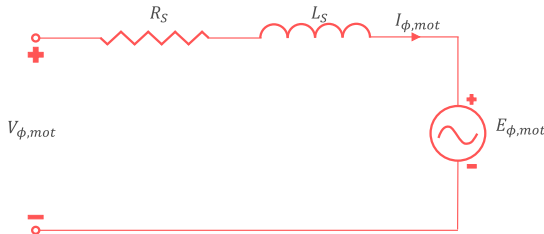


Fig. 8: Phase-wise equivalent circuit of a PMSM.

The back electromotive force $E_{\phi,mot(q)}$ in the motor is calculated using:

$$E_{\phi,mot(q)} = K_e \cdot \omega_{rotor} = \frac{\omega_{rotor}}{K_v} \quad (32)$$

where ω_{rotor} represents the rotor speed, K_e is the back EMF constant (Vs/rad), and K_v is the motor constant provided by the manufacturer (rpm/V).

The no-load torque (Q_{nl}) and the electromechanical torque (Q_{em}) are determined by the following equations:

$$Q_{nl} = \frac{P_{mech}}{\omega_{rotor}} \quad (33)$$

$$Q_{em} = Q_{rotor} + Q_{nl} \quad (34)$$

where P_{mech} is the mechanical power loss of the motor and Q_{rotor} is the load torque from the propeller.

When field weakening is not applied ($I_{\phi,mot(d)} = 0$), the magnitude of the phase current is estimated as:

$$|I_{\phi,mot}| = I_{\phi,mot(q)} = \frac{Q_{em}}{3 \cdot K_e} = \frac{Q_{em} \cdot K_v}{3} \quad (35)$$

The components of the d-axis and q-axis voltages are described as:

$$V_{\phi,mot(d)} = -\omega_{rotor} \cdot n_{pp} \cdot L_s \cdot I_{ph,mot(q)} \quad (36)$$

$$V_{\phi,mot(q)} = E_{\phi,mot(q)} + R_s \cdot I_{\phi,mot(q)} \quad (37)$$

The phase voltage magnitude is then calculated by:

$$|V_{\phi,mot}| = \sqrt{V_{\phi,mot(d)}^2 + V_{\phi,mot(q)}^2} \quad (38)$$

The total power loss (P_{loss}) and input power ($P_{in,mot}$) are given by:

$$P_{loss} = P_{cu} + P_{mech} \quad (39)$$

$$P_{in,mot} = P_{loss} + Q_{rotor} \cdot \omega_{rotor} \quad (40)$$

The modulation index (m_a) is defined as:

$$m_a = 2\sqrt{2} \cdot \frac{|V_{\phi,mot}|}{V_{DC}} \quad (41)$$

where V_{DC} is the DC bus voltage.

In our study, mechanical losses like windage, friction, and stray losses, which generally account for a minor portion of total power losses, were deemed negligible in line with existing literature [51, 52, 53]. Consequently, we equated mechanical losses to copper losses when assessing efficiency. Our analysis focused on copper losses due to their substantial role in total losses, as highlighted in previous research [54].

$$P_{cu} = 3 \cdot R_s \cdot |I_{\phi,mot}|^2 \quad (42)$$

5) *Propeller Model*: We have developed an in-house propeller analysis code based on blade element momentum theory (BEMT) Glauert [55], which combined blade element theory with momentum theory. We incorporate suggested techniques in our code to improve its accuracy and robustness. In the next section, we detail the mathematical modeling of these theories, along with the methods employed for these improvements.

Blade Element Theory: This approach involves the blade element analysis, where the propeller blade is divided into numerous sections. For each section, lift and drag forces are calculated based on their unique airfoil characteristics and the prevailing operational conditions, similar to the force dynamics on an aircraft wing. These forces are then resolved along the propeller's axis, as depicted in Figure 9, to determine the propeller's resultant thrust and torque. The forces generated by an elemental blade section are mathematically represented as axial force (dT) and angular force (dQ). These forces, acting in a plane perpendicular to the blade, are derived from the differential lift (dL) and drag (dD) forces, considering the inflow angle (ϕ):

$$dT = dL \cos \phi - dD \sin \phi \quad (43)$$

$$dQ = dL \sin \phi + dD \cos \phi \quad (44)$$

We further express them in terms of the local resultant wind speed (V_R), chord length (c_r), air density (ρ), and aerodynamic coefficients C_l and C_d :

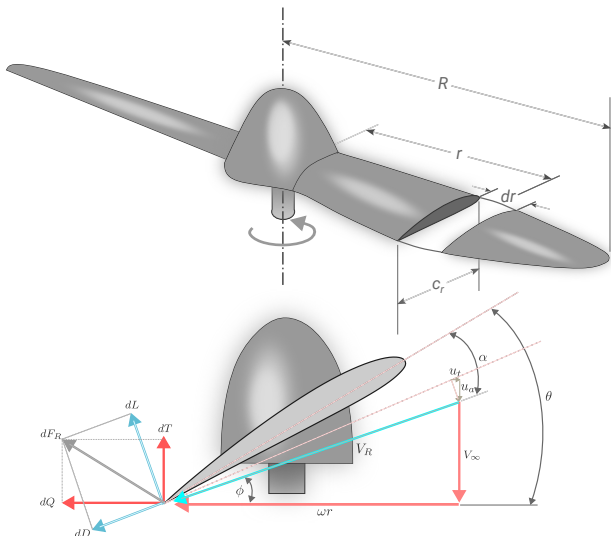


Fig. 9: Propeller analysis using blade element model

$$dT = \frac{1}{2} \rho V_R^2 c_r dr [C_l(\alpha) \cos \phi - C_d(\alpha) \sin \phi] \quad (45)$$

$$dQ = \frac{1}{2} \rho V_R^2 c_r dr [C_l(\alpha) \sin \phi + C_d(\alpha) \cos \phi] \quad (46)$$

V_R and ϕ are calculated using the free stream velocity (V_∞), rotational speed (Ω), and the axial and angular induction factors (a and a'):

$$V_R = \sqrt{[V_\infty(1+a)]^2 + [\Omega r(1-a')]^2} \quad (47)$$

$$\phi = \tan^{-1} \left[\frac{V_\infty(1+a)}{\Omega r(1-a')} \right] \quad (48)$$

The differential thrust (dT) and torque ($d\tau$) are computed as follows:

$$dT = \sigma_r \frac{(1+a)^2}{\sin^2 \phi} [C_l(\alpha) \cos \phi - C_d(\alpha) \sin \phi] V_\infty^2 \rho \pi r dr \quad (49)$$

$$d\tau = \sigma_r \frac{(1+a)^2}{\sin^2 \phi} [C_l(\alpha) \sin \phi + C_d(\alpha) \cos \phi] V_\infty^2 \rho \pi r^2 dr \quad (50)$$

Here, $\sigma_r = \frac{B c_r}{2\pi r}$ represents the blade solidity, with B being the number of propeller blades.

The thrust and torque now can be obtained once we know V_r , C_l , and C_d . We know from Equation 47 that V_R estimation requires a and a' . Therefore, we combine the momentum theory described in the following section to get the induced velocity.

Momentum Theory: Momentum theory is based on conceptualizing the propeller as an actuator disk. This idealization represents the propeller as an infinitely thin disk that induces a minor velocity increment (u) in the flow direction. Fig. 10 provides a clear representation of the actuator disk model in the context of propeller analysis.

The analysis assumes that energy states before and after the propeller remain conserved. Applying Bernoulli's theorem, we can express the pressure difference across the actuator disk as:

$$\Delta p = \frac{1}{2} \rho V_\infty^2 4a(1+a) \quad (51)$$

Here, Δp represents the pressure difference, ρ is the air density, and a is the axial induction factor, quantifying the velocity increment induced by the propeller.

Considering this pressure difference over a small area $dA = 2\pi r dr$ of the disk, the incremental thrust dT is derived:

$$dT = \frac{1}{2} \rho V_\infty^2 4a(1+a)(2\pi r dr) \quad (52)$$

This equation calculates the differential thrust, with r denoting the radial position on the disk.

For the propeller's rotational effects, the incremental torque ($d\tau$) is linked to the change in angular momentum for an elemental annulus of the disk:

$$d\tau = \rho (2\pi r dr) V_d r^2 \omega \quad (53)$$

The angular induction factor, a' , relates to the induced angular velocity (ω) and the propeller disk's angular velocity (Ω):

$$a' = \frac{\omega}{2\Omega} \quad (54)$$

The induced velocity (V_d) through the disk, influenced by a , is:

$$V_d = V_\infty(1+a) \quad (55)$$

Integrating the incremental torque over the entire disk yields the total torque:

$$d\tau = 2a'(1+a)\rho V_\infty \Omega r^3 \pi dr \quad (56)$$

To enhance the accuracy of momentum theory, we incorporate corrections as suggested by Glauert [56], aligning theoretical predictions with empirical data. The tip loss correction factor (\mathcal{F}_T), addressing lift loss at the propeller's tips due to air pressure differences, is calculated as follows:

$$\mathcal{F}_T = \frac{2}{\pi} \cos^{-1} \left[e^{-\frac{B}{2} \left(\frac{R-r}{r|\sin \phi|} \right)} \right] \quad (57)$$

Similarly, the hub loss correction factor (\mathcal{F}_H) accounts for lift loss near the propeller hub:

$$\mathcal{F}_H = \frac{2}{\pi} \cos^{-1} \left[e^{-\frac{B}{2} \left(\frac{r-R_H}{R_H|\sin \phi|} \right)} \right] \quad (58)$$

The combined effect, $\mathcal{F} = \mathcal{F}_T \mathcal{F}_H$, is applied to the disk loading equations (Equations 52 and 56) to align with Blade Element Momentum (BEM) theory solutions (Equations 49 and 50). This yields:

$$\frac{a}{1+a} = \frac{\sigma_r [C_l \cos \phi - C_d \sin \phi]}{4\mathcal{F} \sin^2 \phi} \quad (59)$$

$$\frac{a'}{1+a} = \frac{\sigma_r [C_l \sin \phi + C_d \cos \phi]}{4\mathcal{F} \lambda_r \sin^2 \phi} \quad (60)$$

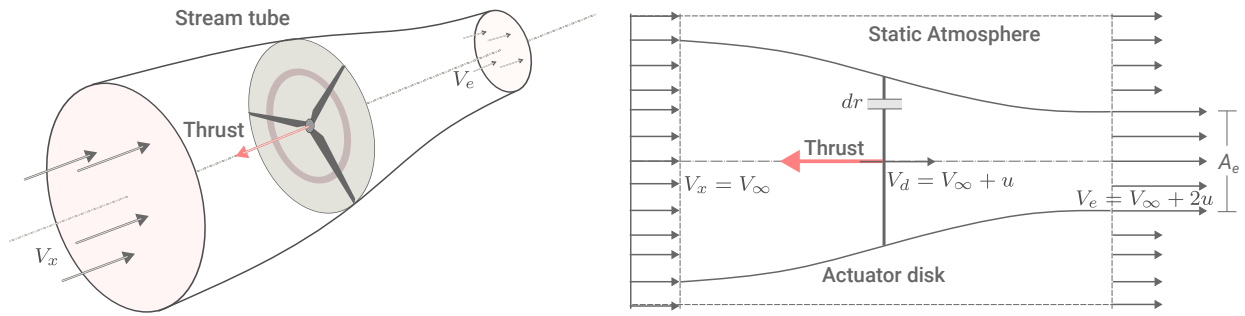


Fig. 10: Schematic of the actuator disk concept used in the momentum theory for analysis of propellers.

where λ_r is the tip speed ratio, which is represented by $\frac{\Omega r}{V_\infty}$.

We utilize XFOIL [57, 58] for pre-stall aerodynamic coefficients estimation and the Viterna method [59] for post-stall extrapolation:

$$C_l = \frac{C_{d_{max}}}{2} \sin 2\alpha + k_l \frac{\cos^2 \alpha}{\sin \alpha} \quad (61)$$

where $C_{d_{max}}$ is the drag coefficient at the angle of attack of 90 degrees. k_l represents a correction factor for lift, calculated based on the stall coefficients. Similarly, the drag coefficient is given by:

$$C_d = C_{d_{max}} \sin^2 \alpha + k_d \cos \alpha \quad (62)$$

For finite aspect ratio blades, $C_{d_{max}}$ varies based on aspect ratio (AR):

$$C_{d_{max}} = \begin{cases} 1.11 + 0.018AR, & \text{if } AR \leq 50 \\ 2.01, & \text{otherwise} \end{cases}$$

The coefficients k_l and k_d are calculated using stall coefficients:

$$k_l = (C_{l_s} - C_{d_{max}} \sin \alpha_s \cos \alpha_s) \frac{\sin \alpha_s}{\cos^2 \alpha_s} \quad (63)$$

$$k_d = C_{d_s} - \frac{C_{d_{max}} \sin^2 \alpha_s}{\cos \alpha_s} \quad (64)$$

To quickly predict C_l and C_d across various Re and angles of attack, we have developed a kriging-based surrogate model and coupled it to the propeller model. Once the values of a and a' are determined, T and τ can be estimated by summing dT and $d\tau$ across the entire blade, respectively. We get the thrust coefficient (C_T) as:

$$C_T = \frac{T}{\rho n^2 D^4} \quad (65)$$

Here, n represents the propeller speed in rotations per second, and D denotes the propeller diameter. We calculate the power coefficient (C_P) as:

$$C_P = \frac{P}{\rho n^3 D^5} \quad (66)$$

P is the power we get from $2\pi n \tau$. We get the efficiency (η) as:

$$\eta = J \frac{C_T}{C_P} \quad (67)$$

where $J = \frac{V}{nD}$, is the advance ratio. The following section briefly discusses the validation study conducted for the motor and propeller model.



Fig. 11: EMRAX 208 [60]: High-efficiency PMSM motor.

IV. MODEL VALIDATION

This section discusses the validation studies of the motor and propeller models.

A. Motor Performance Validation

We conduct a validation of our motor model against the EMRAX 208 [60], an axial flux motor shown in Fig. 11 renowned for its compact and efficient design, making it ideal for electric aircraft applications. Table IX lists the corresponding key motor parameters. This validation process is crucial to ensuring that our motor model accurately reflects the performance characteristics of the EMRAX 208, thereby confirming its suitability for integration into the propulsion system of our electric aircraft design.

Fig. 12 illustrates the EMRAX 208 motor's performance, showcasing peak power and torque over varying speeds. The motor operates efficiently within its Maximum Torque per Ampere (MTPA) range and Flux-weakening (FW) regimes for optimal power [61]. Manufacturer data [60] are plotted alongside our model's performance curves. Notably, peak torque (orange) diminishes with increasing speed, while peak power (blue) rises to a plateau. Power loss (green) escalates with speed. The close alignment between the model and

TABLE III: EMRAX 208HC CC PMSM Parameters [60]

Parameters	Values
Continuous Power (P_{cont}), [kW]	25-40
Peak Power (P_{peak}), [kW]	80
Continuous Torque (Q_{cont}), [N.m]	80
Peak Torque (Q_{peak}), [N.m]	150
Continuous Current (I_{cont}), [A]	100
Peak Current (I_{peak}), [A]	200
Rated Speed (ω_{rated}), [RPM]	4500
Maximum Speed (ω_{max}), [RPM]	6000
Torque Constant (K_t), [N.m/A]	0.83
Poles (n_{pole}), [-]	20
Resistance (R_s), [mΩ]	125
Inductance (L_s), [μH]	130
Flux Linkage (ψ_m), [Vs]	0.0393
Back EMF (K_e), [Vs/rad]	15

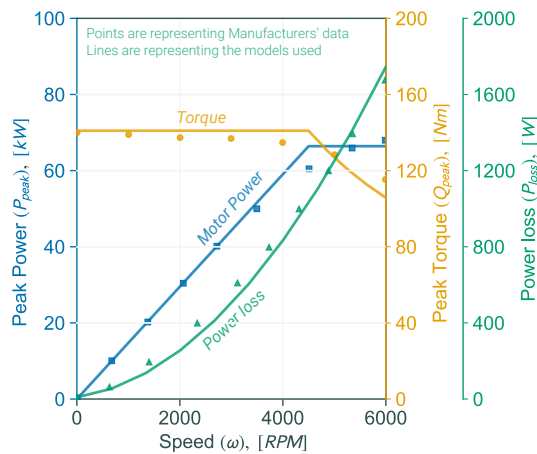


Fig. 12: Peak power, torque, power loss validated with EMRAX manufacturer's data [60]

empirical data assures that the model is acceptable for our use case.

B. Propeller Performance Validation

For validating our propeller model, we utilized experimental data from the study by Adkins and Liebeck [62], with propeller geometrics detailed in Table IV. Given the experimental data's range limitations for advance ratio (J), we further corroborated our model with QBlade [63]. QBlade, a comprehensive open-source simulation software, was initially developed at the Hermann Föttinger Institute of the Technical University of Berlin. It provides robust simulation capabilities that complement our validation process, ensuring the accuracy and reliability of our propeller model.

The graph in Fig. 13 illustrates a comparison of propeller efficiency as a function of advance ratio (J) among three different datasets: our current model, QBlade software simulations [63], and empirical results from Adkins [62].

The plot reveals a strong agreement across these sources, validating the accuracy of the present model against well-established experimental data, as well as QBlade simulations. Therefore, our model is reliable enough to predict propeller performance. However, we further verify the other output parameters to ensure the accuracy, as shown in Fig. 14.

TABLE IV: Propeller's geometry [62]

Radial position (r), [m]	Chord (c_r), [m]	Twist (β_r), [°]
0.5000	0.3424	58.3125
0.8958	0.4605	41.8645
1.2917	0.4269	32.2669
1.6875	0.3569	22.2978
2.0833	0.2796	18.7971
2.4792	0.1913	15.9619
2.8750	0.0000	13.8552

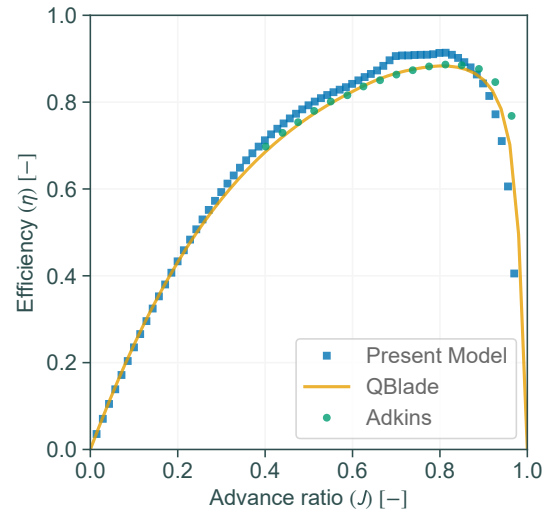


Fig. 13: Efficiency curve for the selected propeller

The provided plots offer a comparative analysis of our model for the thrust coefficient, power coefficient, and torque against the advance ratio (J), labeled respectively as Fig.14a, Fig.14b, and Fig.14c. While overall alignment is observed across these metrics, reinforcing the model's credibility, there is a noticeable deviation at lower values of J . This deviation is attributed to the high angle of attack at lower J , where flow prediction carries inherent uncertainties. Nevertheless, this discrepancy is not expected to significantly impact the model's overall performance due to its occurrence at the corresponding lower vehicle speed.

In the next section, we discuss a case study to demonstrate the efficacy of the proposed method.

V. BOX-WING UAM AIRCRAFT: A CASE STUDY

This section presents our ongoing development of an in-house box-wing UAM aircraft as a case study. We begin by outlining the essential design requirements and mission specifications. A presentation of the initial sizing results follows this. Subsequently, we select appropriate components, which are then incorporated into the resizing process. Finally, we analyze and discuss the results obtained through our framework in detail.

A. Design Requirements and Mission Specifications

Top-level requirements for our UAM study, inspired by Uber Elevate's research [64], encompass aspects such as mission

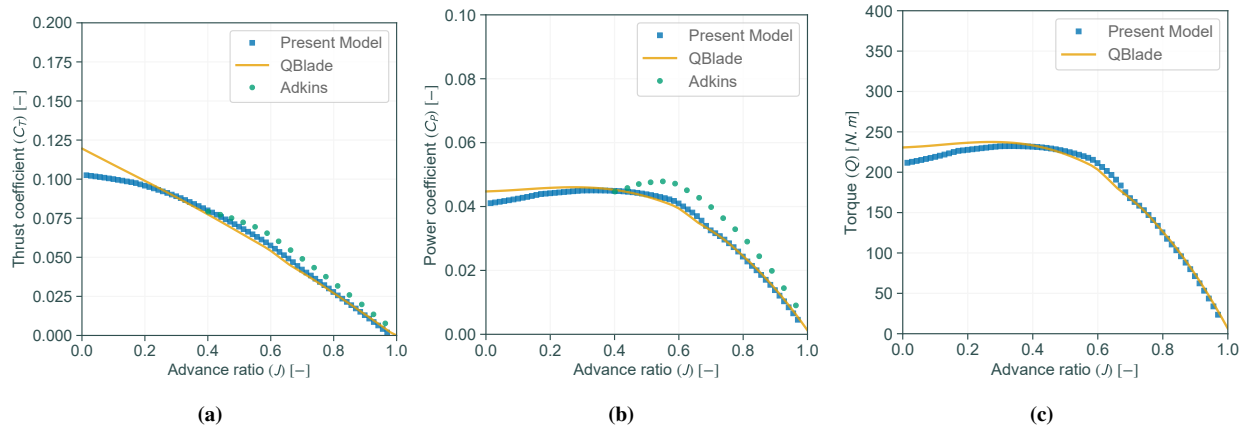


Fig. 14: Performance comparison of the propeller model: (a) Thrust coefficient vs. Advance ratio, (b) Power coefficient vs. Advance ratio, (c) Torque vs. Advance ratio,

TABLE V: TLAR requirements

Parameter	Value
MTOW, [kg]	1500
Seat number	4
Payload, [kg]	444.5
Maximum speed, [m/s]	≥ 73.06
Stall speed, [m/s]	≤ 26.6
Rate of climb, [m/s]	≥ 5.8
Vertical takeoff& landing, [m/s]	≥ 3
Cruise altitude, [ft]	AGL 1500

profile, performance, payload capacity, safety, and various constraints. The mission profile, illustrated in Fig. 15, is crafted based on these comprehensive studies. Additionally, a reserve mission of 6 miles (9.66 km) is integrated into the mission as specified by Uber [64]. Key performance parameters, e.g., maximum rate of climb, cruise speed, and vertical takeoff and landing speeds, are deduced from competitor analysis (Table V) and baseline requirement data [65]. The maximum takeoff and payload masses are determined based on user requirements. In line with Uber Elevate’s specifications [64], we adopt a full payload target of 990 lbs (≈ 444.5 kg), considering average weights for male and female passengers.

B. Configuration Selection and Constant Parameters

A box-wing configuration UAM is selected in this study [15], [66]. This design effectively minimizes induced aerodynamic drag, making it an ideal candidate for integrating hybrid-electric propulsion systems. Previous research has underscored the potential of the box-wing design in the regional aircraft sector, where adopting hybrid-electric propulsion is most promising due to current limitations in battery energy density for medium-long range flights [15]. Our conceptual study aims to explore this integration, particularly for developing emission-free urban and regional aircraft, a technically feasible prospect within the next decade. The choice of a box-wing configuration for Urban Air Mobility (UAM) is further justified by its suitability for hybrid energy usage, combining battery systems for vertical flight and hydrogen fuel cells for

TABLE VI: Key parameters for initial sizing

Parameters	Value
Main wing aspect ratio (AR_{main}), [-]	7.2
Rear wing aspect ratio (AR_{rear}), [-]	6.57
Sweep angle (Δ_{LE}), [°]	20
Mass fraction airframe ($MF_{airframe}$), [-]	0.30
Maximum lift coefficient (C_{Lmax}), [-]	1.4412
Zero-lift drag (C_{D0}), [-]	0.02907
Oswald efficiency (e), [-]	0.86
Figure of Merit (FoM), [-]	0.70
induced factor (k_i), [-]	1.15
solidity (σ), [-]	0.267
blade drag coeff. (Cd), [-]	0.01
Cruise propeller efficiency ($\eta_{propcruise}$), [-]	0.85
Climb propeller efficiency ($\eta_{propclimb}$), [-]	0.70
Takeoff propeller efficiency ($\eta_{propVTOL}$), [-]	0.70
Hover propeller efficiency ($\eta_{prophover}$), [-]	0.50
Motor efficiency (η_{motor}), [-]	0.95
converter/inverter efficiency ($\eta_{inv/conv}$), [-]	0.98
Battery efficiency (η_{batt}), [-]	0.90
Dead of discharge (DoD), [-]	0.80
Battery specific energy (E_{batt}^*), [Wh/kg]	300
Battery specific power (P_{batt}^*), [W/kg]	980

forward flight [67], with proven efficacy in scale-down model flight tests [68, 69, 70]. This selection aligns with our goal to design a highly efficient, environmentally friendly aircraft, addressing both aerodynamic design issues [71] and the physics-based challenges of box-wing configurations [72, 73].

A baseline configuration is shown in Fig 16. Table VI enlists all the key parameters we consider in our study.

C. Results of Initial Sizing

We use the design parameters outlined in Table VI and carry out initial sizing to meet performance and mission requirements. The constraint diagram and the resultant design point of the sizing are depicted in Fig 17. For the forward flight propulsion system, we select the design point based on a power-to-weight ratio (P/W) of 14.13 W/N and a wing loading (W/S) of 627.72 N/m², suitable for forward flight constraints. However, our tilting propulsion system design necessitates satisfying both forward and vertical flight constraints. The hovering and vertical takeoff constraints,

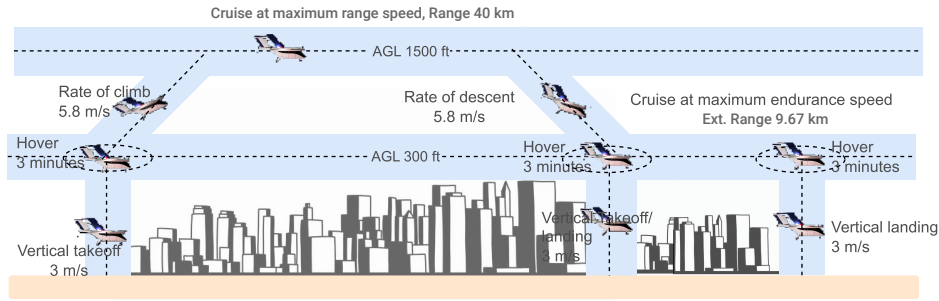


Fig. 15: Sizing design mission

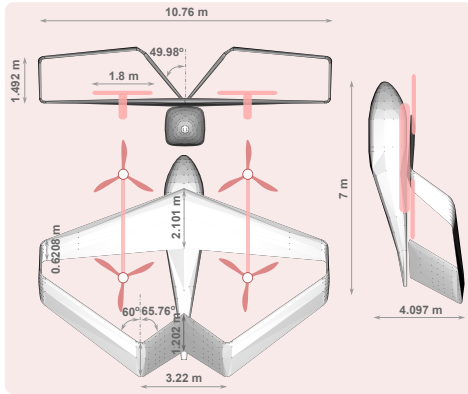


Fig. 16: Our box-wing UAM configuration with key dimensions

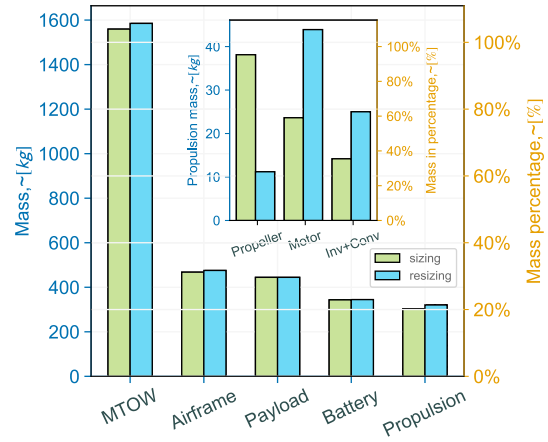


Fig. 18: Initial sizing and resizing mass breakdown

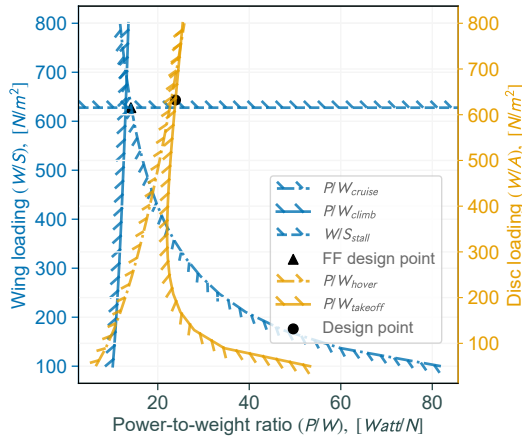


Fig. 17: Constraint analysis and sizing design point

influenced by disc loading, require a specific wing loading to meet fixed-wing stall speed constraints. We identify a disc loading (W/A) of 632.13 N/m^2 and a P/W of 23.88 W/N for minimizing the maximum takeoff mass (MTOW). Consequently, the design point that satisfies both flight modes is at P/W of 23.88 W/N , W/S of 627.72 N/m^2 , and W/A of 632.13 N/m^2 .

The selected design point is crucial for sizing the propulsion system. We estimate battery mass and calculate the total aircraft mass according to our sizing methodology, as depicted in Fig. 2. After the initial sizing phase, we conduct an iterative resizing by selecting suitable propeller, motor, and inverter types. Key parameters identified during this phase

include propeller diameter, motor torque, and RPM, which are essential to meet the point performance requirements. Our initial selection resulted in a propeller diameter of 2.77 m , with each propeller weighing approximately 38.19 kg and the motor weighing 23.62 kg . However, a larger diameter propeller paired with a low-torque motor of the same weight failed to meet our requirements. Consequently, we opted for a smaller propeller diameter of 1.8 m , effectively reducing the propeller mass.

Fig. 18 presents the mass breakdowns for both the initial sizing and resizing phases, showing the changes in the reference vehicle weight of 1500 kg . This iterative approach ensures that our propulsion system components are optimized to meet the specific performance criteria of our aircraft design.

Table VII presents the results of initial sizing and resizing results.

D. Component Selection for Propulsion System

The details of the selected propulsion components are presented in Table VIII. Our analysis utilizes three distinct Tesla battery cell types, each prominently featured in various Tesla vehicle models. The 4680 cell type, known for its high energy density and efficiency, is currently used in the Tesla Model Y. The 2170 cell, offering a balanced blend of power and capacity, is the choice for the Tesla Model 3. Lastly, the 18650 cell, renowned for its reliability and longevity, has been integral to the Tesla Model S, Model X, and the Roadster.

TABLE VII: Initial sizing and resizing results

Parameters	Initial sizing	Resizing
wing loading (W/S), [N/m^2]	627.71	627.71
power-to-weight ratio (P/W), [$Watt/N$]	23.8796	54.02
disc loading (W/A), [N/m^2]	632.12	1527.91
maximum takeoff mass ($MTOM$), [kg]	1559.35	1585.01
Wing area (S_{total}), [m^2]	24.36	24.76
Wing area front (S_{front}), [m^2]	15.83	16.09
Wing area rear (S_{rear}), [m^2]	8.52	8.66
Span front (b_{front}), [m]	10.67	10.76
Propeller diameter (D_{prop}), [m]	2.77	1.8
Propeller mass (M_{prop}), [kg]	38.19	11.2
Motor mass (M_{motor}), [kg]	23.624	43.9
Inverter mass (M_{inv}), [kg]	7.0369	12.5
Converter mass (M_{conv}), [kg]	7.145	12.5
Battery mass (M_{batt}), [kg]	343.35	344.59
Airframe mass ($M_{airframe}$), [kg]	467.80	475.50
Motor power-to-weight ratio (P^*_{motor}), [kW/kg]	3.87	4.78
Constraints	Initial sizing	Resizing
Stall speed (V_{stall}), [m/s]	26.66	26.66
Maximum cruise speed (V_{max}), [m/s]	88.162	116.6
Rate of climb (ROC_{max}), [m/s]	19.34	23.15
Vertical takeoff rate (V_{VTOL}), [m/s]	3.0	12.85

These cells, with their proven performance in electric vehicles, provide a solid foundation for assessing the efficacy of our electric aircraft design.

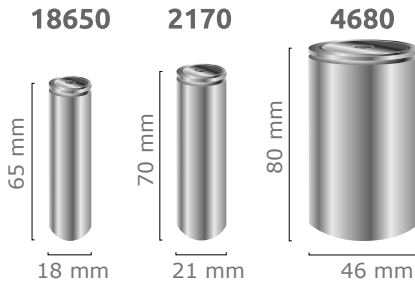


Fig. 19: Cells form factor

Our Box-Wing aircraft employs the 'Cruise Efficient Short Takeoff and Landing' (CESTOL) propeller, a cutting-edge design initially developed by NASA for the Maxwell X-57, an all-electric aircraft [75]. This propeller made of MH117 airfoil sections is designed to enhance cruising efficiency. Adopting the CESTOL propeller in our Box-wing aircraft aligns with our commitment to advanced aerodynamic efficiency and environmental sustainability. Fig. 20 describes the geometry of our 1.8 m diameter propeller.

Fig. 21 shows the scale model, a UAV variant, of the conceptualized Urban Air Mobility (UAM) aircraft during a flight test. This model is a crucial component of the ongoing development for the UAM Operational Digital Twin project [76].

E. Performance and Mission Analysis

Performance and mission analysis are essential to evaluate the aircraft, encompassing the propulsion system and aerodynamics, weight, and other critical disciplines. We examine the impact of the propulsion system and its components

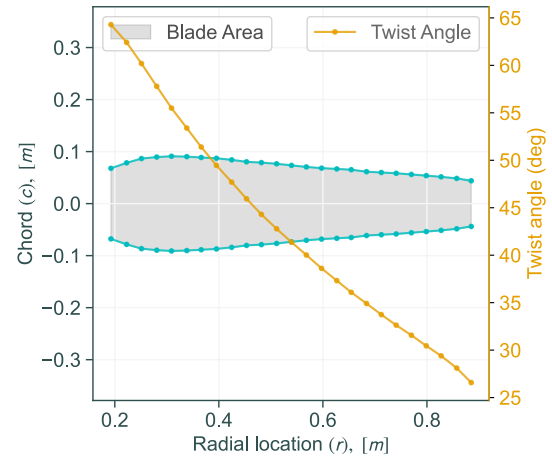


Fig. 20: Box-Wing propeller blade geometry [$pitch = 0^\circ$]



Fig. 21: Scale model of box-wing aircraft during flight test

based on the performance and mission analysis results. The aerodynamics analysis for forward flight is carried out using friction code [77] and AVL [78], while vertical flight dynamics are assessed using the flat plate method. Although weight analysis is not the focus of this paper, the initial sizing weight breakdown results are utilized for designing the battery and selecting other propulsion components.

We define different sets based on product and design data to investigate the performance characteristics of various propulsion systems. A series of case studies listed in Table XI examine the effects of propeller pitch and battery cell characteristics while keeping the propeller diameter and battery mass constant.

Fig. 22 presents an overview of the power requirements for an eVTOL aircraft across various phases of flight. It shows significant peaks in power demand during the takeoff and climb phases, stressing the critical energy needs for vertical lift and altitude gain. During the cruise phase, power requirements stabilize, indicating more efficient energy use. While climb phase power needs are lower than for take-off and landing, motor power peaks since only two motors operate during climb and cruise.

1) *Effect of propeller pitch:* We studied the effects of varying propeller pitch angles for the baseline case. This study analyzed key point performance parameters such as maximum

TABLE VIII: Baseline Propulsion Set

Sets	Propeller	Motor	Inverter	Converter	Cell
Baseline	Pitch 0°	EMRAX348-LV	Brusa DMC534	Dilong DE5000RF-600S28RCA	Tesla 4680

TABLE IX: Cell Parameters [74]

Cell Model	18650	2170	4680
Nominal Energy, [Wh]	13.32	18.23	96
Nominal Voltage, [V]	3.7	3.7	3.7
Total Capacity, [Ah]	3.6	4.8	26.14
Cell Mass, [kg]	0.050	0.070	0.355

TABLE XI: Summary of Case Studies

Study	Propeller Pitch	Cell
Effect of Propeller Pitch	0° - 6°	Tesla 4680
Effect of Battery Cell Types	0°	Tesla 2170, 4680, 18650
Effect of Cell Energy Density	0°	Tesla 4680 ($\pm 10\% E^*$)
Effect of Zero-Lift Drag	0°	Tesla 4680 ($\pm 10\% C_{D_0}$)

TABLE X: Parameters of Converter and Inverter

Component	Parameter	Value
Converter	Nominal capacity (<i>mAh</i>)	3350
	Nominal output voltage (<i>V</i>)	3.6
	Maximum current (<i>A</i>)	10
Inverter	Minimum current (<i>A</i>)	2
	Mass (<i>kg</i>)	0.048
	Rated rotational speed (<i>rad/s</i>)	3660
	Rated voltage (<i>V</i>)	22.2
	Rated current (<i>A</i>)	103

speed, cruise speed, throttle requirement, and maximum take-off rate. We observed significant impacts on maximum thrust and power availability by setting the throttle at 95% and varying the pitch angle from 0 to 6 degrees. As depicted in Fig. 23a and Fig. 23b, an increase in pitch angle leads to higher thrust and power availability, consequently enhancing the maximum speed achievable in forward flight. This highlights the critical influence of pitch angle on the aircraft's point performance, even when electrical components remain unchanged.

In Fig. 23d, we analyze the tip Mach number across varying speeds, focusing on cruise conditions for maximum range and endurance, where the tip Mach number approaches 0.25. At maximum speed, the tip speed Mach number nears 0.9 for a propeller with zero-pitch, indicating that the propeller and motor selection for our aircraft operates efficiently under cruising conditions. This indicates the propulsive components' suitability and performance efficacy, highlighting their optimal functioning within the desired operational envelope.

As illustrated in Fig. 23a, the throttle setting required for cruise flight increases with the propeller's pitch angle Fig. 23c. This leads to a higher current draw, negatively impacting the aircraft's range and endurance, as depicted in Fig. 24a. Consequently, a greater propeller pitch angle results in a reduction of both range and endurance. Furthermore, Fig. 24b reveals that a higher pitch angle contributes to an enhanced maximum rate of climb. These findings highlight the significant influence of propeller pitch angle on key performance parameters, such as cruise efficiency, range, endurance, and climbing capability.

In the context of vertical flight, as depicted in Fig. 25a and Fig. 25b, an increase in propeller pitch necessitates greater thrust and power availability. Consequently, with higher pitch angles, the required throttle setting and power drawn from the power supply are comparatively lower.

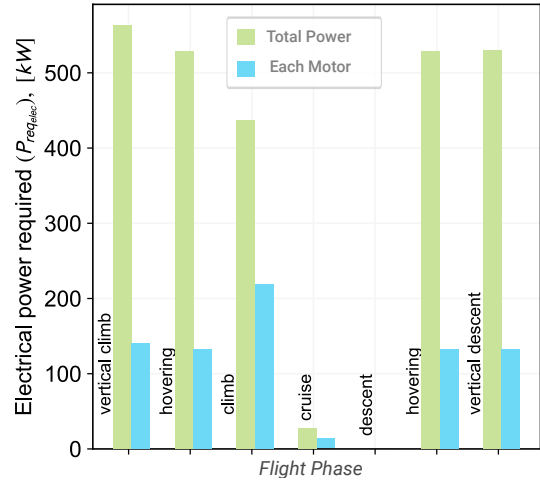


Fig. 22: Electrical power requirement at the various flight phases

2) *Effect of cell types:* Our analysis focuses on the impact of different battery cell types on aircraft performance, examining both point performance and mission responses in various flight modes. We begin by calculating the required number of battery cells, arranging them in series and parallel configurations to align with the motor's maximum voltage specifications and a packing efficiency of 75%. The specific arrangements for Tesla battery cell models — 2170 (cell1), 18650 (cell2), and 4680 (cell3) — are detailed in Table XII. This methodical approach allows us to systematically explore how each cell type influences the aircraft's overall performance. This comparative analysis underscores the significant variations in cell count and configuration necessary to achieve a uniform battery mass with different cell types.

TABLE XII: Comparison of Battery Pack's Cell Arrangements

Cell Model	Energy Density [Wh/kg]	Number of Cells (Series × Parallel)	Total Mass [kg]
2170	260.43	130 × 28	344.59
4680	270.42	130 × 6	344.59
18650	266.40	130 × 40	344.59

Our analysis evaluates each flight mode based on the required thrust and specific flight conditions, as detailed in Section II. While different cell types do not significantly impact point performance parameters like maximum speed, rate of climb, and vertical takeoff speed, their influence is

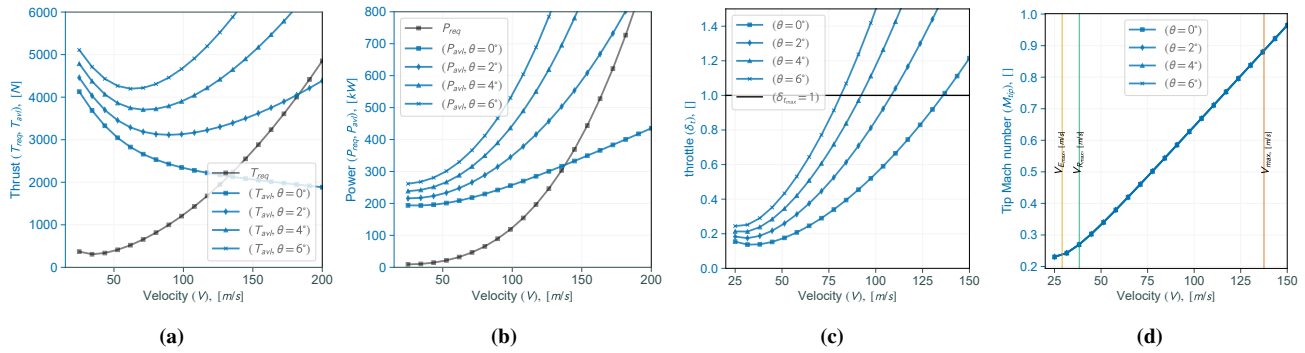


Fig. 23: Effect of propeller pitch on performance in forward flight: (a) Thrust available at various propeller pitches, (b) Power available at various propeller pitches, (c) Throttle setting needed for corresponding propeller pitch setting, and (d) Propeller tip speed at various aircraft speeds.

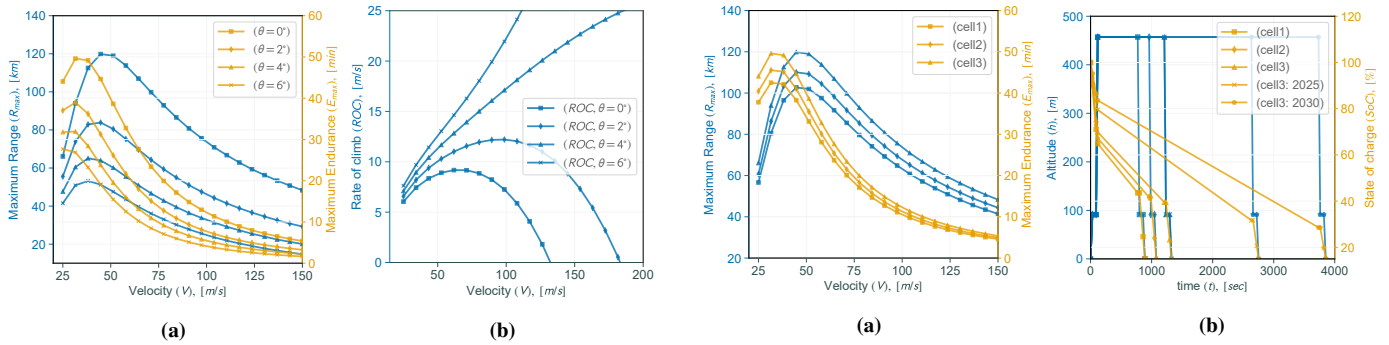


Fig. 24: Effect of propeller pitch on operation: (a) Range and Endurance obtained with different propeller pitches and (b) Rate of climb at various propeller pitches.

Fig. 26: Effect of cell types on the aircraft operation: (a) Range and Endurance obtained with different cells (b) SoC at various stages of flight with different cells

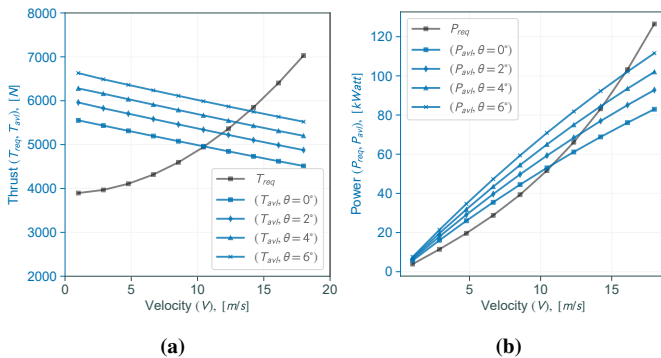


Fig. 25: Effect of propeller pitch on performance in vertical flight: (a) Thrust available at various propeller pitches and (b) Power available at various propeller pitches.

noticeable in aspects of maximum range, endurance, and mission analysis, as demonstrated in Fig. 26a and Fig. 26b.

Comparing different Tesla battery cell models, the 4680 model (cell3) notably achieves the highest range of approximately 120 km and an endurance of 50 minutes. In contrast, the 2170 model (cell1) exhibits the lowest range and endurance, around 105 km and 45 minutes, respectively. Maintaining the same total battery mass of 344.57 kg, the variation in cell types markedly affects the maximum range and endurance. The 4680 model delivers superior performance with a cell mass of 0.355 kg and an energy content of 96

Joules. On the other hand, the 2170 model, with a lighter cell mass of 0.07 kg and an energy content of 18.23 Joules, shows comparatively lower performance due to requiring a higher number of cells than the 4680 model (cell3).

Our mission analysis evaluates the effect of different battery cell types, focusing on SoC history across the mission profile, as illustrated in Fig. 26b. Each mission segment, based on the mission profile (refer Fig. 15), is analyzed, excluding the reserve mission segment. This exclusion is due to the inability of the current battery mass and cell, particularly the 2170 cell type, to complete even the nominal mission.

The analysis shows that a significant portion of SoC is consumed during hover and cruise segments. Notably, during just 1 minute of hovering, SoC drops dramatically from 100% to around 65%. In contrast, the 25-minute cruise segment, which requires less power, leads to a more gradual SoC decrease to approximately 39%, 41%, and 43% for the Tesla models 4860 (cell3), 18650 (cell2), and 2170 (cell1), respectively. The subsequent hover and landing segments consume about 38% SoC, allowing the 4860 model (cell3) to complete a 22-minute mission, the 2170 model (cell1) a 14-minute mission, and the 18650 cell type an 18-minute mission.

Furthermore, we explored a trade-off analysis for future energy density improvements in the 4860 (cell3) model. Based on projections from Amici et al. [79], battery energy density is anticipated to reach 400 Wh/kg by 2025 and 500 Wh/kg by

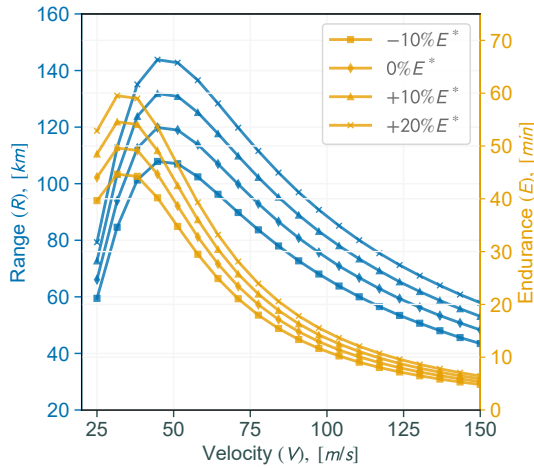


Fig. 27: Range and endurance for ($\pm 10\%$) uncertainty of cell energy density

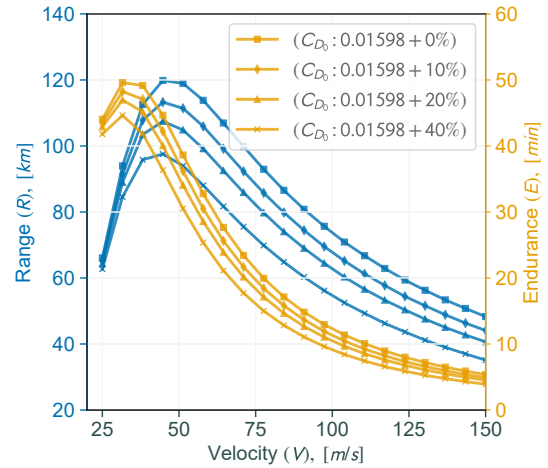


Fig. 28: Range and endurance for increasing zero-lift drag

2030. Under these advancements, while maintaining the same vehicle and battery cell weight, the aircraft's endurance could extend to approximately 45 minutes for 2025 and 64.2 minutes for 2030 battery technology.

3) *Effect of cell energy density:* We also examined the uncertainty in cell energy density and its effects on maximum range and endurance. This analysis, focused on the 4860 cell type (cell1), considers an energy density variation of $\pm 10\%$ from the specified 270.422 Wh/kg. The corresponding outcomes are depicted in Fig. 27. The results indicate that a 10% decrease in cell energy density reduces the maximum range from 120 km to approximately 110 km and a reduction of maximum endurance from 50 minutes to around 45 minutes. Conversely, a 10% increase in cell energy density yields a proportional enhancement in both range and endurance by about 10% compared to the baseline cell configuration. This study underscores that cell energy density is directly proportional to the maximum range and endurance of the aircraft.

4) *Effect of zero-lift drag:* We explore the effects of increasing zero-lift drag on the aircraft's maximum range and endurance, as illustrated in Fig. 28. Keeping propulsion components the same as the baseline, we observed that an increase in zero-lift drag is directly proportional to decreases in both range and endurance. Specifically, elevating zero-lift drag by increments of 10%, 20%, and 40% correspondingly reduced range and endurance by approximately the same percentages. This finding underscores the significant influence of airframe and aerodynamic design on aircraft performance, independent of battery, propeller, or motor component changes.

F. Comments on the Analysis Results

We discuss the key findings from our case study:

- Our initial sizing approach, using empirical equations and historical data, meets design and mission requirements by estimating propulsion size, wing area, and maximum takeoff mass. However, selecting propulsion components may necessitate iterative adjustments to align with performance requirements. We found that a higher diameter

propeller paired with a lower torque motor underperforms, whereas a smaller propeller with a higher torque motor better meets performance criteria. This underscores the importance of balancing motor and propeller torque and RPM in electric aircraft design.

- Propeller pitch significantly influences both point and mission performance. Higher-pitch propellers require increased throttle to achieve the necessary thrust, reducing range and endurance. This finding highlights the critical role of propeller pitch in performance optimization.
- While battery cell types do not significantly impact point performance parameters, they are crucial for achieving maximum range and endurance in mission analysis. We can achieve nominal missions by utilizing current technology's energy density, but reserve missions remain challenging. Our SoC history analysis indicates that higher mass and energy density cells are more effective in fulfilling specific mission requirements.
- The study reveals that cell energy density is pivotal in determining mission success, range, and endurance. An increase in energy density while maintaining cell weight directly enhances these performance metrics, demonstrating a direct proportionality between energy density and mission capability.
- Zero-lift drag directly impacts both mission and point performance. An increase in zero-lift drag leads to a proportional decrease in range and endurance, suggesting that drag reduction technologies could be beneficial, independent of propulsion system modifications.
- Our study suggests that designing with current battery technology and planning for future enhancements is more practical than waiting for hypothetical advances. By accepting a compromise in the initial range, we can extend it later with battery advancements. This approach ensures feasible design and adaptability for future technology upgrades.

G. Limitations of Our Studies

The presented study effectively validates our framework with a box-wing UAM aircraft, proposing future explorations across varied configurations such as thrust vectoring systems, multi-copter designs, and tilted-wing models. Our current focus on available technologies and parameters may limit advancements in range and speed. Furthermore, simplifications in motor loss modeling, alongside unexplored control algorithm efficiencies and thermal management, could influence real-world framework applications. The omission of battery health modeling, wing-propeller interactions, and DEP implications also points to essential directions for future research, underscoring the comprehensive and practical enhancement of our framework.

VI. CONCLUSION

Our study introduces an innovative framework for Advanced Air Mobility (AAM) aircraft design, prioritizing the early integration of electric propulsion to overcome the limitations of traditional methods. By seamlessly merging aircraft sizing with propulsion, and integrating detailed mathematical modeling of propulsion components, our approach enhances design robustness while avoiding impractical outcomes.

The box-wing case study underscores the critical interplay between propulsion system selection, propeller dynamics, and battery technology in AAM design. Notably, careful adjustment of propeller pitch is essential for optimizing mission performance, considering its impact on throttle requirements, range, and endurance. Aligning propulsion components and battery architecture with realistic weight considerations and current technology fosters adaptability to technological advancements.

Our framework's flexibility across different model fidelities ensures its applicability to diverse design scenarios. While successful with the lift+cruise box-wing UAM aircraft, future research avenues include exploring configurations like tilted wings, thrust vectoring, and multicopters. Additionally, detailed analyses of thermal management systems and enhanced battery models to consider health deterioration over time are imperative for accurate estimations.

Moreover, our framework facilitates systematic and adaptable design approaches for electric aircraft, particularly those with distributed electric propulsion. By enabling exploration of various configurations, it holds promise for reducing design and development timelines by preempting unfeasible designs, all while remaining compatible with evolving electric propulsion technologies.

In summary, our study not only advances AAM design methodologies but also lays the groundwork for future innovations in electric propulsion, promising continued evolution alongside technological advancements in the field.

ACKNOWLEDGMENT

This research was supported by the Basic Science Research Program through the National Research Foundation of Korea (NRF) funded by the Ministry of Education (No.2020R1A6A1A03046811).

REFERENCES

- [1] L. Dray, A. W. Schäfer, C. Grobler, C. Falter, F. Allroggen, M. E. J. Stettler, and S. R. H. Barrett, "Cost and emissions pathways towards net-zero climate impacts in aviation," *Nature Climate Change*, vol. 12, no. 10, pp. 956–962, Oct. 2022.
- [2] R. Lindsey, "Climate Change: Atmospheric Carbon Dioxide | NOAA Climate.gov," <https://www.climate.gov/news-features/understanding-climate/climate-change-atmospheric-carbon-dioxide>, May 2023, (Accessed on 10/24/2023).
- [3] U. Nations, "The paris agreement," <https://www.un.org/en/climatechange/paris-agreement>, December 2015, (Accessed on 10/24/2023).
- [4] IEA, "CO2 emissions in aviation in the net zero scenario, 2000-2030 – charts – data & statistics - iea," <https://www.iea.org/data-and-statistics/charts/co2-emissions-in-aviation-in-the-net-zero-scenario-2000-2030>, July 2023, (Accessed on 10/24/2023).
- [5] C. Talwar, I. Joormann, R. Ginster, and T. S. Spengler, "How much can electric aircraft contribute to reaching the Flightpath 2050 CO2 emissions goal? A system dynamics approach for european short haul flights," *Journal of Air Transport Management*, vol. 112, p. 102455, Sep. 2023.
- [6] Q. Long, J. Ma, F. Jiang, and C. J. Webster, "Demand analysis in urban air mobility: A literature review," *Journal of Air Transport Management*, vol. 112, p. 102436, Sep. 2023.
- [7] J. Rohacs and D. Rohacs, "Energy coefficients for comparison of aircraft supported by different propulsion systems," *Energy*, vol. 191, p. 116391, Jan. 2020.
- [8] T. Donato, A. Ficarella, L. Spedicato, A. Arista, and M. Ferraro, "A new approach to calculating endurance in electric flight and comparing fuel cells and batteries," *Applied Energy*, vol. 187, pp. 807–819, Feb. 2017.
- [9] I. Chakraborty and A. A. Mishra, "Sizing of Tilt-Wing Aircraft with All-Electric and Hybrid-Electric Propulsion," *Journal of Aircraft*, vol. 60, no. 1, pp. 245–264, Jan. 2023.
- [10] R. de Vries, M. Brown, and R. Vos, "Preliminary Sizing Method for Hybrid-Electric Distributed-Propulsion Aircraft," *Journal of Aircraft*, vol. 56, no. 6, pp. 2172–2188, Nov. 2019.
- [11] C. A. Saias, I. Goulos, I. Roumeliotis, V. Pachidis, and M. Bacic, "Preliminary Design of Hybrid-Electric Propulsion Systems for Emerging Urban Air Mobility Rotorcraft Architectures," *Journal of Engineering for Gas Turbines and Power*, vol. 143, no. 11, Oct. 2021.
- [12] D. Lee, D. Lim, and K. Yee, "Generic Design Methodology for Vertical Takeoff and Landing Aircraft with Hybrid-Electric Propulsion," *Journal of Aircraft*, vol. 59, no. 2, pp. 278–292, Mar. 2022.
- [13] A. Wendorff, A. Variyar, C. Ilario, E. Botero, F. Capristan, J. Smart, J. Alonso, L. Kulik, M. Clarke, M. Colonna, M. Kruger, J. M. Vegh, P. Goncalves, R. Erhard, R. Fenrich, T. Orta, T. St. Francis, T. MacDonald, T. Momose, T. Economon, T. Lukaczyk, and W. Maier, "SUAVE: An Aerospace Vehicle Environment for Designing Future Aircraft," 2020. [Online]. Available: <https://github.com/suavecocode/SUAVE>
- [14] M. A. Rendón, C. D. Sánchez R., J. Gallo M., and A. H. Anzai, "Aircraft Hybrid-Electric Propulsion: Development Trends, Challenges and Opportunities," *Journal of Control, Automation and Electrical Systems*, vol. 32, no. 5, pp. 1244–1268, Oct. 2021.
- [15] K. Abu Salem, G. Palaia, and A. A. Quarta, "Review of hybrid-electric aircraft technologies and designs: Critical analysis and novel solutions," *Progress in Aerospace Sciences*, vol. 141, p. 100924, Aug. 2023.
- [16] S. L. Schnulo, J. C. Chin, R. D. Falck, J. S. Gray, K. V. Papatthakis, S. Clarke, and N. Reid, "Development of a Multi-Phase Mission Planning Tool for NASA X-57 Maxwell."
- [17] S. Li, C. Gu, P. Zhao, and S. Cheng, "A novel hybrid propulsion system configuration and power distribution strategy for light electric aircraft," *Energy Conversion and Management*, vol. 238, p. 114171, Jun. 2021.
- [18] S. Ma, S. Wang, C. Zhang, and S. Zhang, "A method to improve the efficiency of an electric aircraft propulsion system," *Energy*, vol. 140, pp. 436–443, Dec. 2017.
- [19] J. Park, D. Lee, D. Lim, and K. Yee, "A refined sizing method of fuel cell-battery hybrid system for eVTOL aircraft," *Applied Energy*, vol. 328, p. 120160, Dec. 2022.
- [20] B. L. Litherland, N. K. Borer, and N. S. Zawodny, "X-57 "Maxwell" High-Lift Propeller Testing and Model Development."
- [21] K. Cong, D. Ma, L. Zhang, X. Xia, and Y. Yao, "Design and analysis of passive variable-pitch propeller for VTOL UAVs," *Aerospace Science and Technology*, vol. 132, p. 108063, Jan. 2023.
- [22] J. Wu, F. Gao, S. Li, and F. Yang, "Conceptual Design and Optimization of Distributed Electric Propulsion General Aviation Aircraft," *Aerospace*,

- vol. 10, no. 5, p. 387, May 2023.
- [23] S. S. Chauhan and J. R. A. Martins, "Tilt-Wing eVTOL Takeoff Trajectory Optimization," *Journal of Aircraft*, vol. 57, no. 1, pp. 93–112, Jan. 2020.
- [24] D. Aláez, X. Olaz, M. Prieto, J. Villadangos, and J. J. Astrain, "VTOL UAV digital twin for take-off, hovering and landing in different wind conditions," *Simulation Modelling Practice and Theory*, vol. 123, p. 102703, Feb. 2023.
- [25] M. N. Boukoberine, Z. Zhou, and M. Benbouzid, "A critical review on unmanned aerial vehicles power supply and energy management: Solutions, strategies, and prospects," *Applied Energy*, vol. 255, p. 113823, Dec. 2019.
- [26] M. Wang, S. Zhang, J. Diepolder, and F. Holzapfel, "Battery package design optimization for small electric aircraft," *Chinese Journal of Aeronautics*, vol. 33, no. 11, pp. 2864–2876, Nov. 2020.
- [27] T. Donato and H. Çinar, "Conceptual design and sizing optimization based on minimum energy consumption of lift-cruise type eVTOL aircraft powered by battery and fuel cell for urban air mobility," *Journal of Physics: Conference Series*, vol. 2385, no. 1, p. 012072, Dec. 2022.
- [28] A. M. Kamal and A. Ramirez-Serrano, "Generalized sizing methodology for hybrid aircraft using integrated performance constraints," *Journal of Aircraft*, vol. 56, no. 5, pp. 2083–2092, 2019.
- [29] J. Gundlach, *Designing unmanned aircraft systems*. American Institute of Aeronautics & Astronautics, 2014.
- [30] S. Gudmundsson, *General aviation aircraft design: Applied Methods and Procedures*. Butterworth-Heinemann, 2013.
- [31] G. J. Leishman, *Principles of helicopter aerodynamics*. Cambridge university press, 2006.
- [32] D. Raymer, *Aircraft design: a conceptual approach*. American Institute of Aeronautics and Astronautics, Inc., 2012.
- [33] B. J. Brelje and J. R. Martins, "Electric, hybrid, and turboelectric fixed-wing aircraft: A review of concepts, models, and design approaches," *Progress in Aerospace Sciences*, vol. 104, pp. 1–19, 2019.
- [34] W. Zhou, Y. Zheng, Z. Pan, and Q. Lu, "Review on the Battery Model and SOC Estimation Method," *Processes*, vol. 9, no. 9, p. 1685, Sep. 2021.
- [35] Y. Wang, J. Tian, Z. Sun, L. Wang, R. Xu, M. Li, and Z. Chen, "A comprehensive review of battery modeling and state estimation approaches for advanced battery management systems," *Renewable and Sustainable Energy Reviews*, vol. 131, p. 110015, Oct. 2020.
- [36] Y. Zhao, P. Stein, Y. Bai, M. Al-Siraj, Y. Yang, and B.-X. Xu, "A review on modeling of electro-chemo-mechanics in lithium-ion batteries," *Journal of Power Sources*, vol. 413, pp. 259–283, 2019.
- [37] D. Ramsey, R. German, A. Bouscayrol, and L. Boulon, "Comparison of equivalent circuit battery models for energetic studies on electric vehicles," in *2020 IEEE Vehicle Power and Propulsion Conference (VPPC)*. IEEE, 2020, pp. 1–5.
- [38] N. Campagna, V. Castiglia, R. Miceli, R. A. Mastromauro, C. Spataro, M. Trapanese, and F. Viola, "Battery models for battery powered applications: A comparative study," *Energies*, vol. 13, no. 16, p. 4085, 2020.
- [39] X. Ding, D. Zhang, J. Cheng, B. Wang, and P. C. K. Luk, "An improved thevenin model of lithium-ion battery with high accuracy for electric vehicles," *Applied Energy*, vol. 254, p. 113615, 2019.
- [40] O. Tremblay and L.-A. Dessaint, "Experimental validation of a battery dynamic model for ev applications," *World electric vehicle journal*, vol. 3, no. 2, pp. 289–298, 2009.
- [41] Wikipedia, "DC-to-DC converter," https://en.wikipedia.org/wiki/DC-to-DC_converter, 2023, accessed on 10 18, 2023.
- [42] Z. Zheng, L. Zhang, W. Song, S. Feng, H. Xu, J. Sun, S. Yang, T. Chen, J. Wei, and K. J. Chen, "Gallium nitride-based complementary logic integrated circuits," *Nature Electronics*, vol. 4, no. 8, pp. 595–603, 2021.
- [43] M. Meneghini, C. De Santi, I. Abid, M. Buffolo, M. Cioni, R. A. Khadar, L. Nela, N. Zagni, A. Chini, F. Medjdoub *et al.*, "Gan-based power devices: Physics, reliability, and perspectives," *Journal of Applied Physics*, vol. 130, no. 18, 2021.
- [44] N. Keshmiri, D. Wang, B. Agrawal, R. Hou, and A. Emadi, "Current status and future trends of gan hemts in electrified transportation," *IEEE Access*, vol. 8, pp. 70553–70571, 2020.
- [45] M. Duffy, A. Sevier, R. Hupp, E. Perdomo, and S. Wakayama, "Propulsion scaling methods in the era of electric flight," in *2018 AIAA/IEEE Electric Aircraft Technologies Symposium (EATS)*. IEEE, 2018, pp. 1–23.
- [46] X. Zhang, C. L. Bowman, T. C. O'Connell, and K. S. Haran, "Large electric machines for aircraft electric propulsion," *IET Electric Power Applications*, vol. 12, no. 6, pp. 767–779, 2018.
- [47] Max, "The beginner's guide to permanent magnet synchronous motors," <https://www.linquip.com/blog/permanent-magnet-synchronous-motors/>, 2023, accessed on October 12, 2023.
- [48] H. Lin, H. Guo, and H. Qian, "Design of high-performance permanent magnet synchronous motor for electric aircraft propulsion," in *2018 21st International Conference on Electrical Machines and Systems (ICEMS)*. IEEE, 2018, pp. 174–179.
- [49] Z. Cheng, Z. Cao, J. T. Hwang, and C. Mi, "A novel single-turn permanent magnet synchronous machine for electric aircraft," *Energies*, vol. 16, no. 3, p. 1041, 2023.
- [50] J. G. Hayes and G. A. Goodarzi, "Electric powertrain: energy systems, power electronics and drives for hybrid, electric and fuel cell vehicles," 2018.
- [51] G. Burnand, D. M. Araujo, C. Koechli, and Y. Perriard, "Validation by measurements of a windage losses model for very-high-speed machines," in *2017 20th International Conference on Electrical Machines and Systems (ICEMS)*, 2017, pp. 1–4.
- [52] X. Liu, Z. Q. Zhu, and D. Wu, "Evaluation of efficiency optimized variable flux reluctance machine for evs/hevs by comparing with interior pm machine," in *2014 17th International Conference on Electrical Machines and Systems (ICEMS)*, 2014, pp. 2648–2654.
- [53] F. Stanislav, B. Jan, and L. Jiri, "Analytical derivation of induction machine efficiency map," in *4th International Conference on Power Engineering, Energy and Electrical Drives*. IEEE, 2013, pp. 1206–1210.
- [54] A. Mahmoudi, E. Roshandel, S. Kahourzade, F. Vakilipoor, and S. Drake, "Bond graph model of line-start permanent-magnet synchronous motors," *Electrical Engineering*, pp. 1–15, 2022.
- [55] H. Glauret, "Airplane propellers," *Aerodynamic theory*, 1935.
- [56] ———, *Airplane Propellers*. Berlin, Heidelberg: Springer Berlin Heidelberg, 1935, pp. 169–360.
- [57] "XFOIL," <https://web.mit.edu/drela/Public/web/xfoil/>, (Accessed on 10/30/2023).
- [58] M. Drela, "XFOIL: An analysis and design system for low reynolds number airfoils," in *Low Reynolds Number Aerodynamics*, T. J. Mueller, Ed. Berlin, Heidelberg: Springer Berlin Heidelberg, 1989, pp. 1–12.
- [59] L. A. Viterna and D. C. Janetzke, "Theoretical and experimental power from large horizontal-axis wind turbines," NASA Lewis Research Center, Cleveland, OH (United States), Tech. Rep. DOE/NASA/20320-41; NASA-TM-82944, Sep. 1982.
- [60] EMRAX, "Emrax electric motors/generators," https://emrax.com/wp-content/uploads/2017/01/emrax_208_technical_data_4.5.pdf, 2023, accessed on 10 24, 2023.
- [61] M. Li, J. He, and N. A. Demerdash, "A flux-weakening control approach for interior permanent magnet synchronous motors based on z-source inverters," in *2014 IEEE Transportation Electrification Conference and Expo (ITEC)*, 2014, pp. 1–6.
- [62] C. N. Adkins and R. H. Liebeck, "Design of optimum propellers," *Journal of Propulsion and Power*, vol. 10, no. 5, pp. 676–682, Sep. 1994.
- [63] D. Marten, "Qblade: a modern tool for the aeroelastic simulation of wind turbines," 2020.
- [64] U. Elevate, "Uber air vehicle requirements and missions," *Uber Tech. Rep.*, 2018. [Online]. Available: <https://s3.amazonaws.com/uber-static/elevate/Summary+Mission+and+Requirements.pdf>
- [65] Y. Lee, J. Lee, and J.-W. Lee, "Holding area conceptual design and validation for various urban air mobility (uam) operations: A case study in seoul-gyungin area," *Applied Sciences*, vol. 11, no. 22, 2021. [Online]. Available: <https://www.mdpi.com/2076-3417/11/22/10707>
- [66] A. L. Tasca, V. Cipolla, K. Abu Salem, and M. Puccini, "Innovative Box-Wing Aircraft: Emissions and Climate Change," *Sustainability*, vol. 13, no. 6, p. 3282, Jan. 2021.
- [67] A. Jae-hyun, Z. W. Thu, L. Jae-ryun, L. Young-jae, M. Jae-seon, J. Mak-sim, N. Seung-hyuk, and L. Jae-woo, "Performance operation analysis study of hydrogen fuel cell urban air transportation," *Collection of abstracts from the Korean Society of Aeronautics and Astronautics conference*, pp. 663–664, 2020. [Online]. Available: <https://www.dbpia.co.kr/journal/articleDetail?nodeId=NODE10526236>
- [68] J. Hyun, M. Jang, T. A. Nguyen, and J.-W. Lee, "Transition control planning and optimization for a boxed-wing evtol tiltrotor vehicle using trim analysis," in *2023 International Conference on Unmanned Aircraft Systems (ICUAS)*. IEEE, 2023, pp. 1128–1135.
- [69] M. Jang, J. Hyun, T. Kwag, C. Gwak, T. A. Nguyen, and J.-W. Lee, "Uamdyncon-dt: A data-driven dynamics and robust control framework for uam vehicle digitalization using deep learning," in *2023 International Conference on Mechatronics, Control and Robotics (ICMCR)*. IEEE, 2023, pp. 81–85.
- [70] M. Jang, J. Hyun, T. Kwag, C. Gwak, C. Jeong, T. A. Nguyen, and

- J.-W. Lee, "es-dnnc: A deep neural network control with exponentially stabilizing control Lyapunov functions for attitude stabilization of puv," in *2022 22nd International Conference on Control, Automation and Systems (ICCAS)*. IEEE, 2022, pp. 81–86.
- [71] P. Jemmitola and P. Okonkwo, "An Analysis of Aerodynamic Design Issues of Box-Wing Aircraft," *Journal of Aviation Technology and Engineering*, vol. 12, no. 2, Sep. 2023.
- [72] K. Abu Salem, V. Cipolla, G. Palaia, V. Binante, and D. Zanetti, "A Physics-Based Multidisciplinary Approach for the Preliminary Design and Performance Analysis of a Medium Range Aircraft with Box-Wing Architecture," *Aerospace*, vol. 8, no. 10, p. 292, Oct. 2021.
- [73] K. Abu Salem, G. Palaia, A. A. Quarta, and M. R. Chiarelli, "Preliminary analysis of the stability and controllability of a box-wing aircraft configuration," *Aerospace*, vol. 10, no. 10, p. 874, 2023.
- [74] "18650 vs. 21700 Li-ion cells – A direct comparison of electrochemical, thermal, and geometrical properties," *Journal of Power Sources*, vol. 472, p. 228614, Oct. 2020.
- [75] C. B. Hoover, J. Shen, and A. R. Kreshock, "Propeller whirl flutter stability and its influence on x-57 aircraft design," *Journal of Aircraft*, vol. 55, no. 5, pp. 2169–2175, 2018.
- [76] J. L. Lee, M. Tyan, D.-Y. Kwon, and J.-W. Lee, "Enhanced calibration and performance prediction method for entire propulsion system of evtol uav," *IEEE Transactions on Transportation Electrification*, 2023.
- [77] W. H. Mason. (2002) FRICTION skin friction/form factor drag estimation. [Online]. Available: http://www.dept.aoe.vt.edu/~mason/Mason_f/FRICTman.pdf
- [78] M. Drela and H. Youngren. (2022) AVL 3.36 extended vortex-lattice model. [Online]. Available: <https://web.mit.edu/drela/Public/web/avl/>
- [79] J. Amici, P. Asinari, E. Ayerbe, P. Barboux, P. Bayle-Guillemaud, R. J. Behm, M. Berecibar, E. Berg, A. Bhowmik, S. Bodoardo *et al.*, "A roadmap for transforming research to invent the batteries of the future designed within the european large scale research initiative battery 2030+," *Advanced energy materials*, vol. 12, no. 17, p. 2102785, 2022.